1

The interaction of a shock wave with a laminar boundary layer at a compression corner in high-enthalpy flows including real gas effects

By S. G. MALLINSON†, S. L. GAI and N. R. MUDFORD

School of Aerospace and Mechanical Engineering, University College, University of New South Wales, Australian Defence Force Academy, Canberra ACT 2600, Australia

The high-enthalpy, hypersonic flow over a compression corner has been examined experimentally and theoretically. Surface static pressure and heat transfer distributions, along with some flow visualization data, were obtained in a free-piston shock tunnel operating at enthalpies ranging from 3 MJ kg^{-1} to 19 MJ kg^{-1}, with the Mach number varying from 7.5 to 9.0 and the Reynolds number based on upstream fetch from 2.7×10^4 to 2.7×10^5. The flow was laminar throughout. The experimental data compared well with theories valid for perfect gas flow and with other relevant low-to-moderate enthalpy data, suggesting that for the current experimental conditions, the real gas effects on shock wave/boundary layer interaction are negligible. The flat-plate similarity theory has been extended to include equilibrium real gas effects. While this theory is not applicable to the current experimental conditions, it has been employed here to determine the potential maximum effect of real gas behaviour. For the flat plate, only small differences between perfect gas and equilibrium gas flows are predicted, consistent with experimental observations. For the compression corner, a more rapid rise to the maximum pressure and heat transfer on the ramp face is predicted in the real gas flows, with the pressure lying slightly below, and the heat transfer slightly above, the perfect gas prediction. The increase in peak heat transfer is attributed to the reduction in boundary layer displacement thickness due to real gas effects.

1. Introduction

The compression corner is a convenient configuration for examining shock wave/ boundary layer interaction. A schematic of the flow is shown in figure 1. The shock wave due to the corner interacts with the flat-plate boundary layer some distance upstream of the corner. For sufficiently strong shocks, the flow separates and a recirculating region is formed. As the flow reattaches, the boundary layer thickness is reduced and a reattachment shock is formed due to the coalescence of the compression waves. This flow has been widely studied both at supersonic and hypersonic speeds but largely under low-enthalpy conditions where the gas behaves essentially as a perfect gas (see, for example, Gadd 1956; Chapman, Kuehn & Larson 1958; Amick 1959; Curle 1961; Erdos & Pallone 1962; Lees & Reeves 1964; Miller, Hijman & Childs 1964; Holden 1965, 1966, 1967, 1971*a*, 1978; Needham 1965, 1967;

† Present address: Department of Aeronautics, Imperial College of Science, Technology and Medicine, Prince Consort Road, London SW7 2BY, UK.
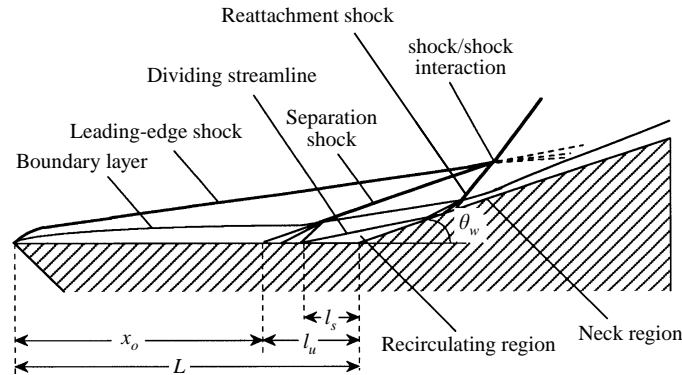
FIGURE 1. Schematic of hypersonic compression corner flow. l_s = upstream separated length; l_u = upstream influence; L = upstream fetch (or flat-plate length); x_o = axial location of the beginning of the interaction = $L - l_u$.

Putnam 1965; Needham & Stollery 1966; Hankey 1967; Anders & Edwards 1968; Harvey 1968; Johnson 1968; Lewis, Kubota & Lees 1968; Klineberg & Lees 1969; Anders 1970; Holden & Moselle 1970; Ball 1971; Carter 1972; Bloy & Georgeff 1974; Hankey & Holden 1975; Hung & MacCormack 1976; Ikawa 1977; Madhavan & Swaminathan 1986; Power & Barber 1986; Délery 1989; Katzer 1989; Rizzetta & Mach 1989; Ramakrishnan, Thornton & Weiting 1991; Rudy *et al.* 1991; Fay & Sambamurthi 1992; Vermeulen & Simeonides 1992; Grasso, Leone & Délery 1994; Simeonides, Haase & Manna 1994; Inger 1994; Kumar & Stollery 1994).

For flow over hypersonic vehicles, the fluid may not always be treated as a perfect gas. In spite of this, little attention has been paid to the problem of shock wave/boundary layer interaction at high-enthalpy hypersonic flow conditions in which real gas phenomena such as vibrational excitation and chemical reaction may proceed and significantly influence the flow (Park 1990). An earlier experimental study (Rayner 1973) found no real gas effects on the flow examined. In contrast, theoretical studies have predicted changes of up to 30% in both separation length and peak heating for real gas flows when compared to perfect gas flows (Ballaro & Anderson 1991; Grasso & Leone 1994; Grumet, Anderson & Lewis, 1994).

This study examines the real gas effects on compression corner flow. Flow over a flat plate at zero incidence is also considered here and is taken as the datum for the compression corner flow being, as it is, a compression corner in the limit as the corner angle approaches zero. Only laminar flows are considered here.

Experiments were conducted using a free-piston shock tunnel facility (Stalker 1972). The pressure and heat transfer distributions along the model surface were measured. Some flow visualization data were also obtained. The local flat-plate similarity theory of Stollery & Bates (1974), valid for perfect gas flows, has been extended to include equilibrium real gas effects. This new theory is used to determine the maximum effect of real gas behaviour on compression corner flow.

2. Experimental details

2.1. *Free-piston shock tunnel and flow conditions*

The present experiments were conducted using the Australian National University free-piston shock tunnel facility, T3 (Stalker 1972). The nozzle reservoir pressure, p_0,

was approximately 22 MPa whilst the total enthalpy, h_0, ranged from 2.8 to 19.1 MJ kg^{-1}. The flow was generated by expanding the high-pressure high-enthalpy reservoir through a conical nozzle with a throat diameter of 12.7 mm, exit diameter of 305 mm and a cone half-angle of 7.5°.

Experiments were conducted at three conditions designated B, D and G following East, Stalker & Baird (1980). The test gas was air. Typical reservoir and free-stream conditions are presented in table 1. The details of the calculation procedure used to obtain these values are presented elsewhere (Mallinson 1994; Mallinson, Gai & Mudford 1996a). The error due to variations in shock speed and reservoir pressure are of the same order as variations due to flow divergence over the model length. These values are for temperature, T_∞: 5%; for pressure, p_∞: 15%; for density, ρ_∞: 12%; for velocity, u_∞: 2%; and for Mach number, M_∞: 3%. The species concentrations vary by less than 0.5%. These are of the same order as or less than the shot-to-shot repeatability (Gai & Joe 1992).

In the calculation of the Reynolds number, $Re_x = \rho_\infty u_\infty x / \mu_\infty$, the coefficient of viscosity, μ_∞, was obtained from a curve fit to values calculated assuming a Lenard–Jones potential (Hirschfelder, Curtiss & Bird 1967). This curve fit has been found (see Mallinson 1994) to compare well with values obtained using the Wilke (1955) mixing rule. The Prandtl number, Pr, does not vary appreciably over the range of conditions tested (Hansen 1959) and was assumed to have a constant value of 0.72.

An examination of the heat transfer records reveals none of the characteristic unsteadiness usually associated with transition to turbulent flow (Kumar & Stollery 1994; Mee & Goyne 1995; Zanchetta 1996). This together with the high Mach number and low to moderate Reynolds number of the present flows suggests that the flow was laminar throughout.

The test time available in free-piston shock tunnels is limited by contamination of the flow by driver gas (Crane & Stalker 1977). It has been shown for the T3 facility that provided the enthalpy does not exceed approximately 25 MJ kg^{-1}, there is sufficient time to establish steady attached flat-plate flow (East *et al.* 1980). The time required for the attainment of steady conditions in a flow containing an embedded separated region generally exceeds that required for the establishment of steady attached flow (Holden 1971b). Mallinson & Gai (1994) demonstrated that, for the present flow conditions, steady separated flow may be established before driver gas contamination becomes a serious problem.

2.2. *Model details*

The flat plate/compression corner model is shown in figure 2. A flat plate and a ramp plate rest upon gauge housings which, in turn, are attached to a support plate. By inserting wedges beneath the housing for the ramp plate, the corner angle can be varied from 5° to 24°. The flat plate model is achieved by removal of the wedge altogether. The heat transfer and pressure measurements were made using separate models. Upwash from the undersurface of the model is prevented by side-skirts extending below the flat plate and ramp plate upper surfaces.

The bow shock associated with the gauge housing may be detached. For large enough detachment distances, this may disturb the flow over the upper surface of the model. The angle of the front face of the gauge housing was set smaller than the shock detachment angle for the present flow conditions, and preliminary flow luminosity visualization data reveal that the bow shock does not interfere with flow over the upper surface of the model.

	h_0 (MJ kg^{-1})	p_0 (MPa)	T_0 (K)	p_∞ (kPa)	T_∞ (K)	ρ_∞ ($\times 10^{-3}$ kg m^{-3})
B	19.0	22.2	8400	0.99	1160	2.60
D	13.7	22.2	7200	0.99	940	3.43
G	2.83	22.4	2400	0.73	160	16.0

	u_∞ (km s^{-1})	M_∞	Re_∞ ($\times 10^5$ m^{-1})	$\gamma_{fr\infty}$	α_O	$1 - \dfrac{h_{chem}}{h_r - h_w}$
B	5.47	7.5	3.10	1.45	0.8	0.85
D	4.20	7.5	4.08	1.43	0.4	0.92
G	2.28	9.1	32.2	1.40	0.0	1.00

TABLE 1. Reservoir and free-stream conditions for the experimental study. h = enthalpy, p = pressure, T = temperature, ρ = density, u = velocity, M = Mach number, Re = unit Reynolds number, γ_{fr} = frozen ratio of specific heats, α_O = oxygen dissociation mass fraction. The subscripts 0 and ∞ refer to conditions in the nozzle reservoir and in the free stream, respectively. Model wall temperature, T_w = 300 K (ambient).
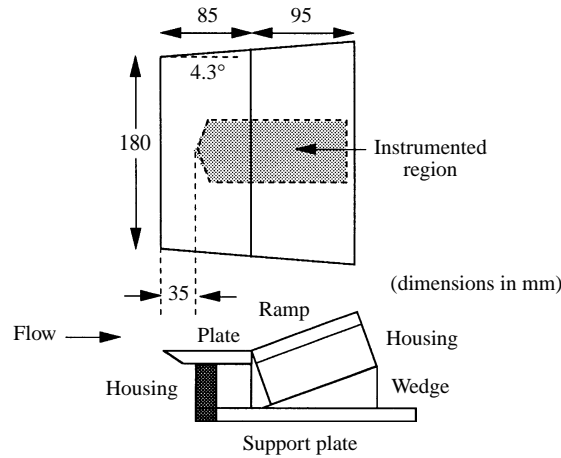

FIGURE 2. The flat plate/compression corner model. The flat-plate configuration is achieved by removing the wedge.

The leading edge had a thickness of not greater than 10 μm, which satisfies the criterion for sharpness proposed by Stollery (1972). Leading-edge bluntness effects are therefore negligible.

The model width is 180 mm, which is 50 mm less than the diameter of the inviscid core of the nozzle. The sides of the plates are inclined so as to be parallel to the source-like flow produced by the conical nozzle. The model length is 180 mm which ensures that it is within the nozzle exit Mach cone.

The junction of the plates was set as close as possible to avoid misalignment. Small misalignments were, however, present, but these were typically less than 10 μm, which is small compared with the boundary layer thickness of approximately 3 mm (Gai *et al.* 1989). Leakage through the corner can decrease the extent of separation (Ball & Korkegi 1968; McIntosh & Hornung 1970; Dumitrescu & Preda 1985; Hahn, Shih & Chyu 1993). To prevent this, the corner was sealed from below with an industrial sealing compound.

2.3. *Consideration of three-dimensional effects*

The compression corner is a nominally two-dimensional fluid dynamics problem. For experiments conducted with finite span models, there may be three-dimensional effects due to, for example, outflow from the sides near the corner. Outflow may be prevented by the use of sidefences. These may introduce further three-dimensional effects and can not be used when obtaining flow visualization data. Therefore, the two-dimensionality of the flow must be examined.

Several studies have found that provided the model aspect ratio is greater than unity, the flow in the midspan region may be considered two-dimensional (Miller *et al.* 1964; Holden 1967; Lewis *et al.* 1968). A more stringent requirement was proposed by Holden & Moselle (1970) whereby a compression corner flow would only be considered two-dimensional if the spanwise and chordwise flows (through distributions of surface pressure and heat transfer) were shown to be unaffected by adding side fences (to prevent spillage) or by successive increases in aspect ratio.

A recent CFD code validation study (Rudy *et al.* 1991) employed the experimental data of Holden & Moselle (1970). For attached and incipiently separated flows, the comparison between two-dimensional calculations and experiment was good. For separated flow, the two-dimensional code proved insufficient. By adopting a three-dimensional implementation of the code, Rudy *et al.* found good agreement with the experimental data, not only in terms of the surface quantities, but also with the time required to establish steady separated flow. Subsequently, Lee & Lewis (1993) found that a comparison between a two-dimensional CFD calculation and the Holden & Moselle data for separated flow was as good as, if not better than, that obtained by Rudy *et al.* using a three-dimensional calculation. This does not imply that the separated flow is purely two-dimensional. It does suggest, however, that the flow in the midspan region may reasonably be considered two-dimensional if it is not affected by addition of side fences or increases in aspect ratio.

To examine whether two-dimensional flow was produced here, the heat transfer was measured on the centreline and at 40 mm either side of the centreline at the same axial location. Experiments were conducted with and without side fences attached to the sides of the model. Figure 3(*a*) shows the time development of heat transfer at two points at the same axial, but different off-centre, locations upstream of the corner within the separated region when side fences are employed. There are some small variations between the signals during the establishment of steady flow. Once a steady state has been reached, the signals are almost identical. The comparison is repeated in figure 3(*b*) for flow without side fences; once again, the on- and off-axis signals are identical in the steady state. When the traces are compared for flow at the same axial and transverse locations with and without side fences attached to the model, the agreement is equally good. From these results, it would appear that two-dimensional flow was achieved in the model midspan region, even for well separated flows.

2.4. *Instrumentation*

2.4.1. *Pressure and heat transfer*

The pressures were measured using PCB 113M165 piezoelectric pressure transducers. These were calibrated in the range 0.5–50 kPa by suddenly applying a known pressure difference to the face of the transducer. The gauge response was linear even at the lower range of the pressures. The transducers were carefully mounted to minimize transmission of stress waves along the model and were recessed 1.5 mm to protect them from the harsh environment of the shock tunnel flow. The pressure
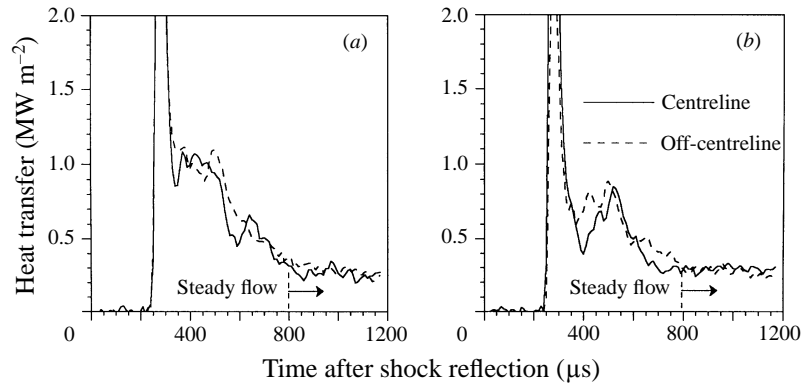
FIGURE 3. Heat transfer signals for centreline and off-centreline locations within the separated region: (*a*) with side fences; (*b*) without side fences.
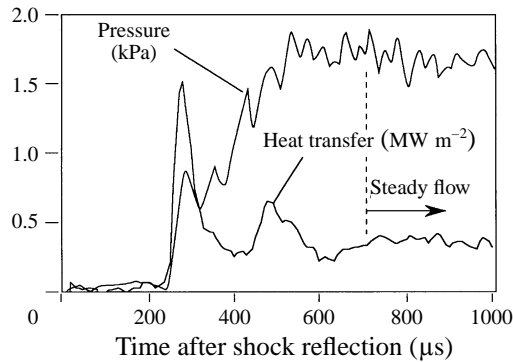

FIGURE 4. Typical unfiltered pressure and heat transfer records.

tappings were 1 mm in diameter. The time required to fill the cavity volume in front of a transducer was calculated to be be approximately 30 μs. The signal presented in figure 4 suggests that the transducer response is satisfactory using the present mounting configuration. The fluctuation in signal levels during the steady flow period was approximately $\pm 10\%$, whilst the fluctuation in the mean was less than $\pm 1\%$.

The heat transfer was obtained using co-axial chromel-alumel (Type 'K') surface junction thermocouples. These devices have been successfully employed in several earlier investigations (Boyce & Mundt 1991; Gai & Joe 1992; Gai, Mudford & Hackett 1992; Gai & Mudford 1992). The heat transfer is inferred from the variation of temperature with time as measured by the thermocouples according to the method of Schultz & Jones (1973). Using the method of Jessen, Vetter & Grönig (1993), the thermocouple thermal product was determined to be $(\rho ck)^{1/2} = 9500 \pm 500$ W s$^{1/2}$ m^{-2} K^{-1}. The uncertainty in heat transfer as measured by these gauges is approximately 15% (Gai & Joe 1992). The fluctuation in the mean signal level during the steady flow period was less than $\pm 2\%$.

The gauge outputs were digitized and directed to a personal computer for analysis. The signal sampling rate was 400 kHz per channel. Typical unfiltered pressure and heat transfer signals are shown in figure 4.

2.4.2. *Flow visualization*

The flow over the compression corner was visualized using a Mach–Zehnder interferometer. There were approximately 80 fringes across the field of view, and the fringes were set at $-60°$ to the incoming flow so that the heterodyne frequency of the fringes did not coincide with any of the flow field information in the Fourier plane. The light source was a flash-lamp pumped dye laser with a wavelength of 589.1 ± 0.6 nm. The laser pulse length was typically 1 µs, which gave stationary fringes in the steady flow period of approximately 300 µs. The interferogram was focused onto a CCD camera and the data stored on a personal computer. The phase distribution, which is related to the density field (Liepmann & Roshko 1957), is obtained by performing a two-dimensional Fourier transform analysis of the interferograms in a manner described by Bone, Bachor & Sandeman (1986) and Boyce *et al.* (1994).

3. Experimental results

3.1. *Flat plate*

There have been several studies of flat-plate flow at similar conditions to those employed in the present study (see, for example, East *et al.* 1980; Gai *et al.* 1989; He 1991; Kelly, Simmons & Paull 1992). It is nevertheless important to examine the flat-plate flow as it is the datum case for the compression corner flow being, effectively, a compression corner flow with zero corner angle.

3.1.1. *Pressure*

Stollery (1970) has found $2A'\bar{\chi}/(\gamma + 1)$ to be an important correlating parameter for flat-plate pressure distributions in hypersonic flow. Here, the hypersonic viscous interaction parameter, $\bar{\chi}$, is given by

$$\bar{\chi} = M_\infty^3 \left(C^* / Re_x \right)^{1/2} \tag{3.1}$$

and

$$A' = 0.332(\gamma - 1) \left(1 + 2.6 T_w / T_0 \right) \tag{3.2}$$

where $C = (\mu/\mu_\infty)(T_\infty/T)$ is the Chapman–Rubesin constant, x is the distance from the leading edge, and γ is the specific heat ratio. The subscript w refers to conditions at the wall and the superscript $*$ refers to conditions evaluated at the Eckert (1955) reference enthalpy, h^*, given by

$$h^* = 0.5 \left(h_e + h_w \right) + 0.22 \left(h_r - h_e \right) \tag{3.3}$$

where the recovery enthalpy, h_r is defined as

$$h_r = h_0 + 0.5 \left(Pr^{*1/2} - 1 \right) u_e^2 \tag{3.4}$$

and the subscript e denotes conditions at the edge of the boundary layer. Typical values of $\bar{\chi}$ at $x = 85$ mm (the hinge line for the compression corner experiments) are 2.28, 1.97 and 1.24 for conditions B, D and G, respectively.

The pressure data from the present flat-plate experiments are compared in terms of $2A'\bar{\chi}/(\gamma + 1)$ in figure 5 with the predictions for laminar flow from flat-plate similarity theory (Stollery 1970; Stollery & Bates 1974), with some perfect gas cold-wall data (Lewis *et al.* 1968; Holden & Moselle 1970; Kumar & Stollery 1994) and with the data from the high-enthalpy experiments of Stacey (1989). All the data appear to be satisfactorily correlated in this form. It should be noted that the success of the
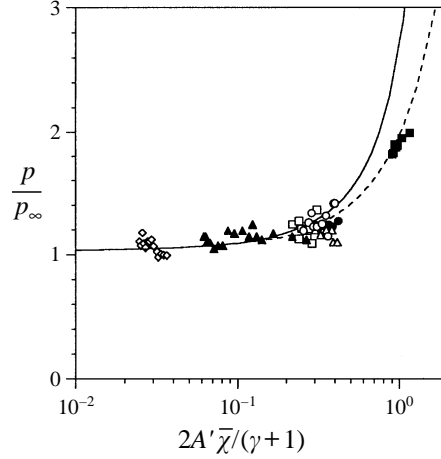
FIGURE 5. Correlation of flat-plate pressures. Symbols represent experimental data: ○, □, △, conditions B, D and G, respectively, present experiments; ◇, Stacey (1989); ●, Lewis *et al.* (1968) ■, Holden & Moselle (1970); ▲, Kumar & Stollery (1994). Curves represent theoretical predictions: ——, Stollery (1970); − − − −, Stollery & Bates (1974).

parameter $2A'\bar{\chi}/(\gamma + 1)$ in correlating the results may be attributed to the fact that it includes both viscous interaction and wall temperature effects.

The predictions from the flat-plate similarity theories of Stollery (1970) and Stollery & Bates (1974) are seen to diverge when $2A'\bar{\chi}/(\gamma + 1) > 0.1$. The latter appears to be in better agreement with experimental data for larger values of $2A'\bar{\chi}/(\gamma + 1)$, that is, in the strong interaction region.

It would seem from figure 5 that the real gas effects present in conditions B and D do not significantly influence the pressure. Note that the frozen value of the ratio of specific heats, γ, was used in figure 5 since the leading-edge shock is weak. Although the pressure along a flat plate can be affected by the presence of vibrational and chemical non-equilibrium, it would appear that these effects are only of second order. This is consistent with previous studies of real gas effects on pressure distributions (Capiaux & Washington 1963; Stalker1989*a*,*b*).

3.1.2. *Heat transfer*

For self-similar boundary layer flow of a perfect gas, the reference enthalpy method combined with Reynolds' analogy gives the heat transfer, q_w, in terms of the Stanton number, St, as (Anderson 1989)

$$St = 0.332(Pr^*)^{-2/3}(C^*)^{1/2}Re_x^{-1/2} \tag{3.5}$$

where

$$St = \frac{q_w}{\rho_e u_e (h_r - h_w)}. \tag{3.6}$$

For free-piston shock tunnel flows, the nozzle expansion may cause the recombination reactions to proceed so slowly that the free-stream flow is in a frozen dissociated state. If this occurs, some of the free-stream enthalpy will be stored as chemical potential enthalpy. This, in turn, will cause the heat transfer to be reduced. When there is no recombination of the atomic species, either in the boundary layer or at the wall, it has been found (East *et al.* 1980; Gai *et al.* 1989) that the heat transfer may be evaluated using the Eckert (1955) reference enthalpy method modified to include
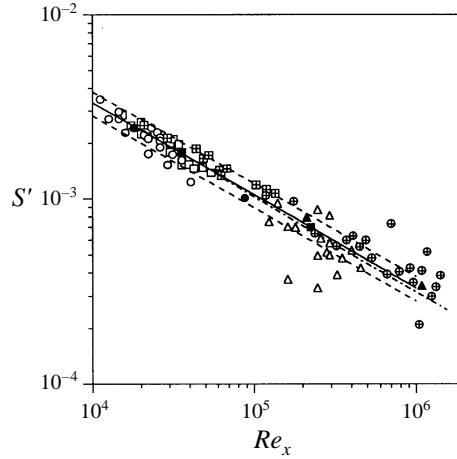
FIGURE 6. Correlation of flat-plate heat transfer. Symbols represent experimental data: ○, □, △, conditions B, D and G, respectively, present experiments; ●, East *et al.* (1980), $h_0 = 22$ MJ kg^{-1}; ■, East *et al.* (1980), $h_0 = 14$ MJ kg^{-1}; ▲, East *et al.* (1980), $h_0 = 3$ MJ kg^{-1}; ⊕, He (1991), $h_0 = 19$ MJ kg^{-1}; ⊞, Hackett (1993). Curves represent theoretical predictions: ——, theory, (3.9); — — — —, ±15% of (3.9); — · — · — · —, Stollery & Bates (1974) theory.

the effects of dissociation in the free stream. The heat transfer at this frozen limit is given by

$$St_{fr} = 0.332(C^*)^{1/2}(Pr^*)^{-2/3}Re_x^{-1/2}\left(1 - \frac{h_{chem}}{h_r - h_w}\right) \qquad (3.7)$$

where h_{chem} is the chemical potential enthalpy due to dissociated species. In the limit of equilibrium boundary layer chemistry, where complete recombination of the atomic species occurs, $h_{chem} = 0$ and the perfect gas expression for heat transfer, (3.5), is obtained.

For the present experiments, it has been found that the flat-plate boundary layer flow is chemically frozen (Mallinson 1994; Mallinson, Gai & Mudford 1996*b*), so that the effects of recombination and dissociation are not significant within the boundary layer. The surface recombination rate is also negligible, suggesting that the heat transfer should be given by (3.7).

Rearranging (3.7) gives

$$St' = 0.332Re_x^{-1/2} \qquad (3.8)$$

where

$$St' = St_{fr}(Pr^*)^{2/3}(C^*)^{-1/2}\left(1 - \frac{h_{chem}}{h_r - h_w}\right)^{-1}. \qquad (3.9)$$

The heat transfer data from the present investigation are compared in the form of (3.8) in figure 6 along with other relevant high-enthalpy data (East *et al.* 1980; He 1991; Hackett 1993), and with the prediction from laminar flat-plate similarity theory (Stollery & Bates 1974).

As can be seen, most of the data lie within a band of 15% from the East *et al.* (1980) theory. Also, the East *et al.* theory and the Stollery & Bates (1974) theories are in close agreement, with small differences appearing as the Reynolds number is increased. The values which lie significantly outside of the 15% band are those of He (1991), which may be due to the flow being transitional, and the condition G data

which suffer from poor signal to noise ratio arising from the low surface heat transfer values on the flat plate. The flows in all the previous investigations were found to be chemically frozen to recombination whilst the increases in h_{chem} due to endothermic processes, as calculated by the method described in Mallinson *et al.* (1996*b*), were found to be negligible.

In summary, from figures 5 and 6, it would appear that the real gas effects on flat-plate flow under the present experimental conditions are small, and that the effect of any endothermic reactions, such as those discussed by East *et al.* (1980), are negligible for the flows considered.

3.2. *Compression corner*

This section presents the pressure and heat transfer distributions and the flow visualization data which were obtained for corner angles of $\theta_w = 5°$, $10°$, $14°$, $15°$, $16°$, $18°$ and $24°$. A complete set of data was not obtained for each corner angle at all three conditions. However, the data are sufficiently comprehensive for the discussion.

For flows that were judged to be attached, incipiently separated or just past incipient separation, the experimental pressure and heat transfer data are compared with the theoretical predictions for laminar flow of a perfect gas as proposed by Stollery & Bates (1974). The theory cannot predict separation as it does not allow for reversed flow profiles. It is therefore not applicable to experimental data for well separated flows.

The error bars shown in the pressure and heat transfer distributions represent $\pm10\%$ and $\pm15\%$, respectively, of the value at the representative locations shown. The determination of these uncertainty levels is discussed in §2.4.1.

3.2.1. *Corner angle* = 5°

The heat transfer data for conditions B, D and G at a corner angle of 5° are shown in figure 7(*a*–*c*), respectively. For all three conditions it appears, notwithstanding the large data scatter, that the heat transfer minimum is sharp. This is typical of attached flows (Needham 1965). Note that there are fewer data points for condition G. This is because several transducers suffered from poor signal to noise ratio and the results from these had to be excluded. The points which are seen to lie well below the others for condition G were obtained from signals which had only marginally better signal to noise ratio than those that were discarded.

The effect of dissociated species in the free stream on the heat transfer was accounted for by multiplying the Stanton number predicted by the Stollery & Bates (1974) laminar perfect gas theory by the factor $\{1 - h_{chem}/(h_r - h_w)\}$ to produce the theoretical Stanton number curve presented here. Note that for condition G, this factor is unity and so the original calculation is shown. The agreement with the theory is considered reasonable, especially in the vicinity of the corner and upstream.

3.2.2. *Corner angle* = 10°

The pressure and heat transfer distributions for conditions B, D and G at a corner angle of 10° are shown in figures 8(*a*–*c*) and 9(*a*–*c*), respectively. The phase distributions for conditions B and D are shown in figure 10(*a*, *b*), respectively.

It is seen that the pressure rises and the heat transfer falls from the flat-plate values at a small distance upstream of the corner. For conditions B and D, the pressure rises almost continuously and the heat transfer minimum seems sharp, notwithstanding the data scatter. These observations are consistent with attached flow. This is supported by
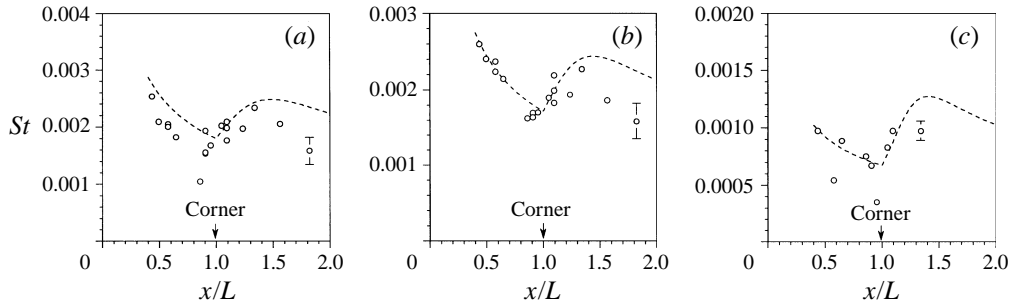
FIGURE 7. Compression corner heat transfer distributions, $\theta_w = 5°$ (upstream fetch, $L = 85$ mm): (*a*) condition B; (*b*) condition D; (*c*) condition G. $\bigcirc$, Experimental data; $----$, Stollery & Bates (1974) perfect gas theory multiplied by $\{1 - h_{chem}/(h_r - h_w)\}$.
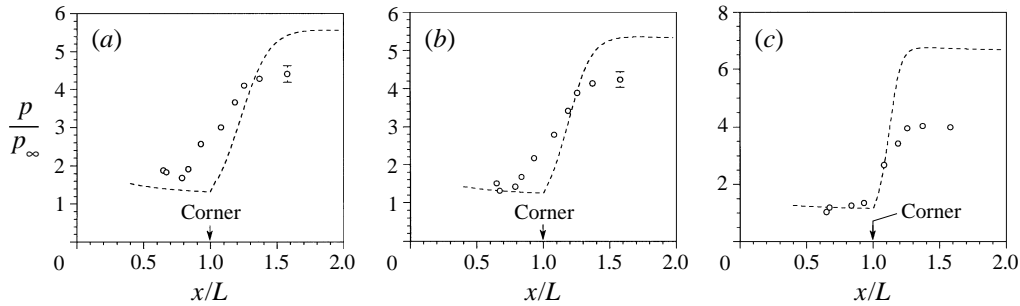

FIGURE 8. Compression corner pressure distributions, $\theta_w = 10°$: (*a*) condition B; (*b*) condition D; (*c*) condition G. $\bigcirc$, Experimental data; $----$, Stollery & Bates (1974) perfect gas theory.
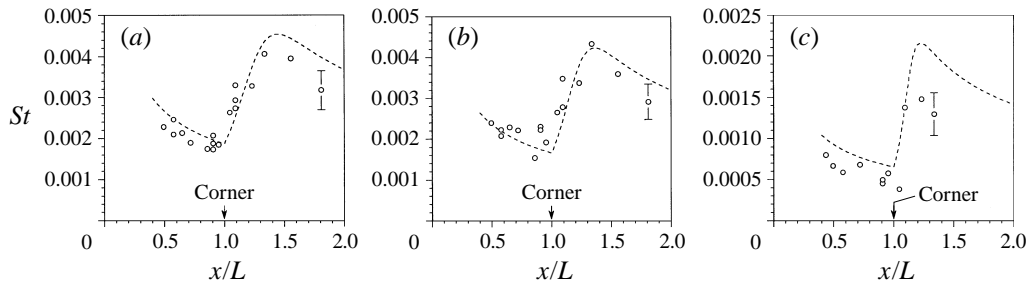

FIGURE 9. Compression corner heat transfer distributions, $\theta_w = 10°$. (*a*) condition B; (*b*) condition D; (*c*) condition G. Refer to figure 7 for explanation of symbols.

the phase distributions which show no separated region. For condition G, there seems to be a slight inflection in the pressure distribution near the corner and it is uncertain whether the heat transfer minimum is rounded or sharp. This indicates that the flow may be near to but not quite at the incipient separation condition (Needham 1965; Délery 1989). There seems moderate to fair agreement between experimental data and the Stollery & Bates (1974) prediction in the corner and upstream regions.

3.2.3. *Corner angle* $= 14°$

The heat transfer distributions for conditions B, D and G at a corner angle of $14°$ are shown in figure 11 (*a–c*), respectively. The minimum in heat transfer for conditions
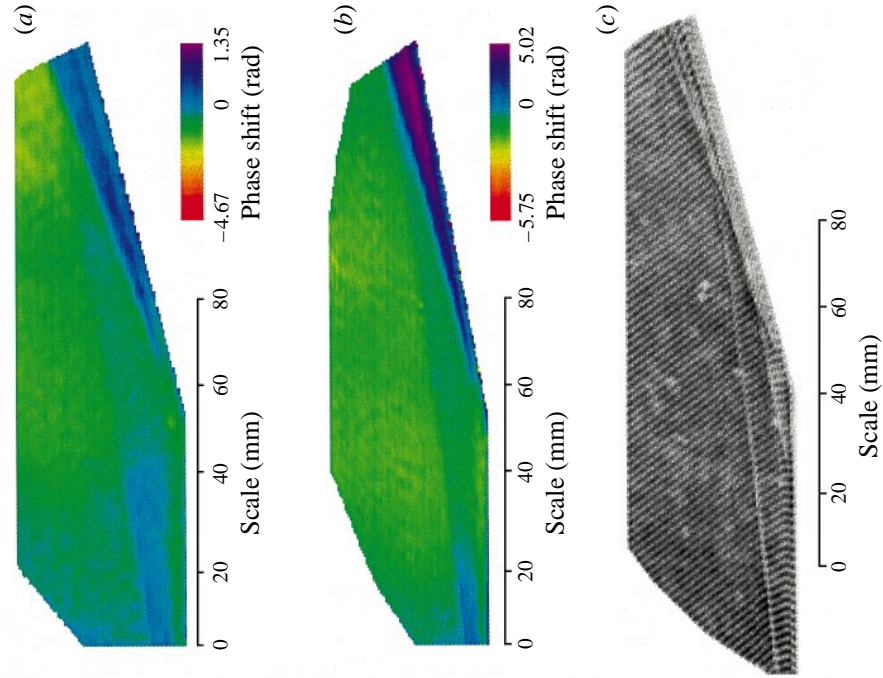
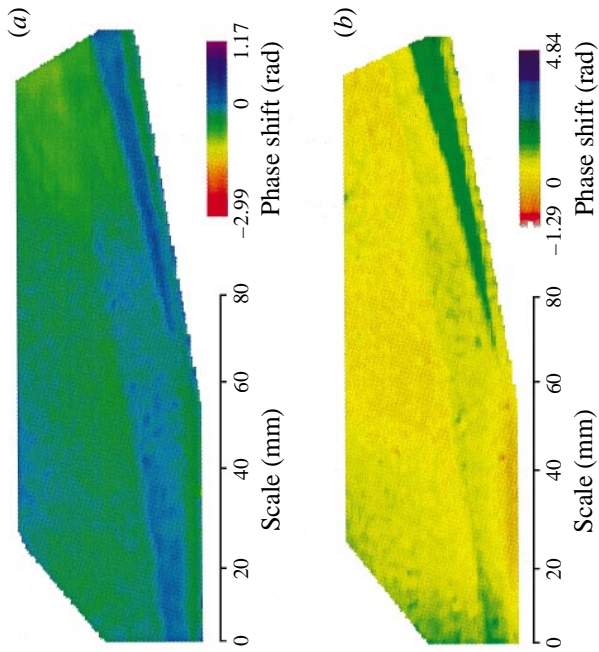FIGURE 14. Flow visualization for $\theta_w = 15°$: (*a*) condition B; (*b*) condition D; (*c*) condition G.

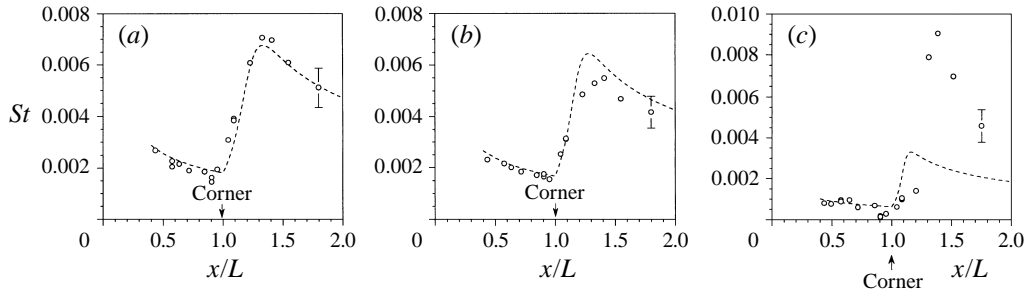FIGURE 10. Flow visualization for $\theta_w = 10°$: (*a*) condition B; (*b*) condition D.

FIGURE 11. Compression corner heat transfer distributions, $\theta_w = 14°$: (a) condition B; (b) condition D; (c) condition G. Refer to figure 7 for explanation of symbols.

B and D still appears to be sharp, whereas there is a rounded minimum for condition G. It is therefore uncertain whether flow at conditions B and D is attached or close to incipient separation whereas it would appear it is separated at condition G. The agreement between the Stollery & Bates (1974) theory and the measurements is good for conditions B and D both upstream and downstream of the corner. The poor agreement between the data and theory in the reattachment region may indicate that the flow is well separated for condition G.

3.2.4. *Corner angle = 15°*

The pressure, heat transfer and phase distributions for conditions B and D at a corner angle of 15° are shown in figures 12(a, b), 13(a, b) and 14(a, b) (see page 12), respectively. The pressure distribution and interferogram for condition G at a ramp angle of 15° are shown in figures 12(c) and 14(c), respectively. There are no heat transfer data for condition G at this wedge angle. The condition-G interferogram contains closely spaced fringes which cannot be resolved using the present analysis and so no phase distribution was produced (D. J. Bone 1994, personal communication).

It could be argued that the pressure distributions for conditions B and D show a small inflection near the corner, whilst a pressure plateau is evident near the corner for condition G. It is difficult to say precisely whether the heat transfer minimum for conditions B and D is sharp or rounded, mainly because there are so few data points upstream of the corner. This was due to a number of thermocouples upstream of the corner experiencing failure during the experiments at this wedge angle. The flow visualization reveals no separation for conditions B and D and a large separated region for condition G. Given the inflection in the pressure distributions for conditions B and D, these flows appear to be incipiently separated. The flow for condition G is clearly separated.

The heat transfer data again compare well with the Stollery & Bates (1974) theory, but the comparison with the pressure is poor. The pressure distribution near reattachment is almost constant for conditions B and D whereas it shows a peak for condition G. The latter is characteristic of the reattachment of a separated flow (Délery 1989).

3.2.5. *Corner angle = 16°*

The heat transfer distributions for conditions B, D and G at a corner angle of 16° are shown in figure 15(a–c), respectively. It is uncertain whether the heat transfer minima for conditions B and D are sharp (indicating attached flow) or rounded (indicating separated flow). This seems to suggest that conditions B and D are near
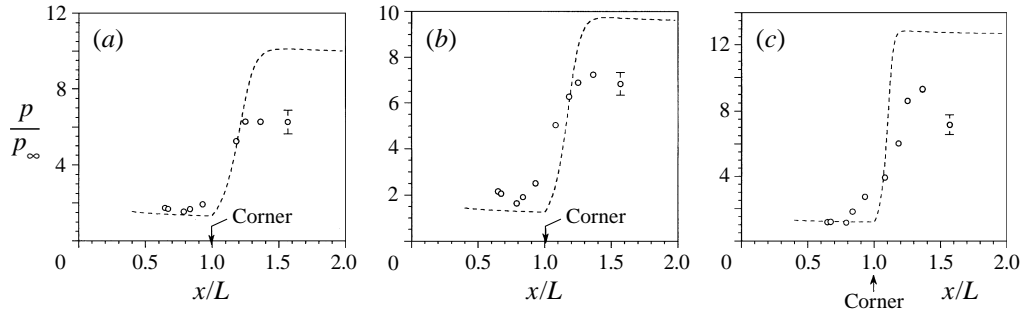
FIGURE 12. Compression corner pressure distributions, $\theta_w = 15°$: (*a*) condition B;
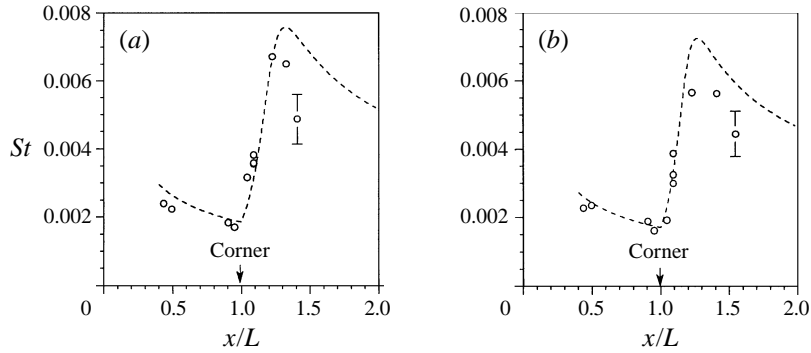(*b*) condition D; (*c*) condition G. Refer to figure 8 for explanation of symbols.

FIGURE 13. Compression corner heat transfer distributions, $\theta_w = 15°$: (*a*) condition B;
(*b*) condition D. Refer to figure 7 for explanation of symbols.

FIGURE 15. Compression corner heat transfer distributions, $\theta_w = 16°$:
(*a*) condition B; (*b*) condition D; (*c*) condition G. Refer to figure 7 for explanation of symbols.

to incipient separation at this corner angle. The heat transfer minimum for condition G appears to be round. The heat transfer distributions for conditions B and D still compare quite well with the Stollery & Bates theory.

3.2.6. *Corner angle* = 18°

The pressure, heat transfer and phase distributions for conditions B, D and G at a corner angle of 18° are presented in figures 16(*a–c*), 17(*a–c*) and 18(*a–c*), respectively. Once again, the interferogram for condition G contains closely spaced fringes which are unresolvable using the present analysis.

FIGURE 16. Compression corner pressure distributions, $\theta_w = 18°$: (*a*) condition B; (*b*) condition D; (*c*) condition G. Refer to figure 8 for explanation of symbols.

The pressure distributions for conditions B, D and G all seem to exhibit a pressure plateau near the corner. It is arguable whether the minima in the heat transfer for conditions B and D are rounded. The minimum in the heat transfer for condition G is definitely rounded. The flow visualizations for conditions B and D show a small separated region near the corner, whilst there is a large region of separated flow for condition G. Thus, the flow lies just past incipient separation for conditions B and D and is well separated for condition G.

A shock/shock interaction can be seen clearly in the interferogram for condition G. It would appear from the flow visualization data that for conditions B and D this interaction occurs downstream of the measurement region. This type of shock/shock interaction has been classified by Edney (1968) as type VI. Separation causes the spreading of the compression waves, which eventually coalesce into a single shock. After this, the flow encounters an expansion fan which causes the pressure to drop giving rise to the apparent peaks in the pressure distributions for conditions B, D and G. The peak in heat transfer is due to localized reductions in the boundary layer thickness (Hung & MacCormack 1976). This type of interaction can also be seen in the flow visualization data for condition G at $\theta_w = 15°$ (figure 14), where its effect would seem to be limited to a region downstream of the instrumented section of the model.

The peaks in pressure and heat transfer seem more pronounced for condition G, which suggests a greater spreading of the compression waves and hence a larger separated region than conditions B and D. Also, in view of its higher Reynolds number, the growth length of the reattaching boundary layer may be smaller for condition G than for conditions B and D, which could also explain the relatively higher heat transfer (Simeonides *et al.* 1994).

The experimental heat transfer compares well with the Stollery & Bates (1974) theory for conditions B and D, whilst the comparison with the pressure is poor. Note that the theory is not appropriate for the flow at condition G because at this angle, the flow is well separated.

3.2.7. *Corner angle* = 24°

The pressure and heat transfer for conditions B, D and G at a corner angle of 24° are presented in figures 19(*a*–*c*) and 20(*a*–*c*), respectively. The phase distributions for conditions B and D are presented in figure 21(*a*, *b*) (see page 17), respectively. The discontinuities in phase for conditions B and D near reattachment are due to the close spacing of fringes. These do not detract from the overall result as it is still possible to see what is occurring near the discontinuities. An infinite fringe interferogram
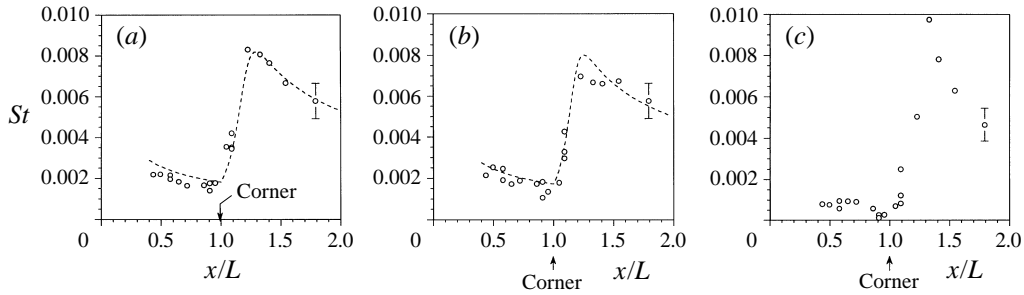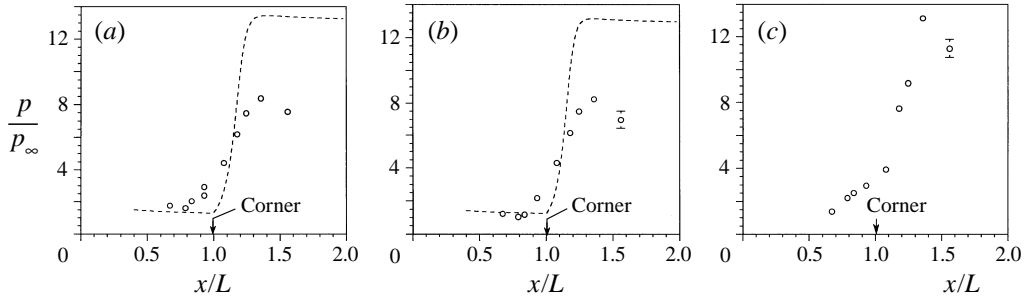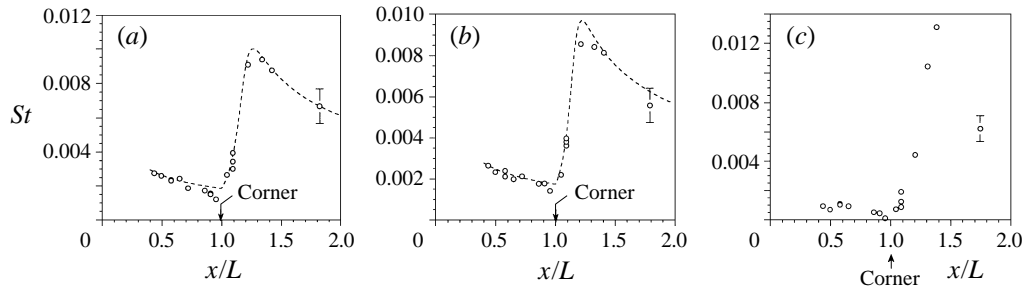
FIGURE 17. Compression corner heat transfer distributions, $\theta_w = 18°$: (a) condition B; (b) condition D; (c) condition G. Refer to figure 7 for explanation of symbols.

for condition B, shown in figure 21(c) (see page 17), seems to display the same flow features as figure 21(a). This is an indication of the validity of the analysis technique applied to the interferograms (Liepmann & Roshko 1957).

The heat transfer minima for conditions B and D are clearly rounded whereas for condition G the heat transfer appears to be nearly constant upstream but rising rapidly downstream of the corner. The reason for this rapid rise may be due to transition to turbulence downstream of separation. This would be unlikely given the high Mach number and moderate Reynolds number of this flow condition, but nevertheless possible. Also shown in figure 20(c) is the prediction for turbulent flow from Stollery & Bates (1974) after reattachment. The reattachment point was taken as the location of peak heating. There are insufficient data downstream to ascertain the likelihood or otherwise of transition. It must be mentioned, however, that the heat transfer signals do not exhibit the characteristic unsteadiness that has been observed in transitional compression corner flows (Kumar & Stollery 1993).

The pressure distributions display distinct plateaus for all three flow conditions. The flow visualization for conditions B and D reveal large separated regions followed by an Edney (1968) type VI shock/shock interaction just past reattachment.

3.2.8. General features of compression corner flow

The pressure and heat transfer distributions for conditions B, D and G, as discussed above, indicate that the interaction spreads and the maxima in the pressure and heat transfer distributions increase as the corner angle is increased.

Also, as the corner angle is increased, the agreement between the experimental data and the perfect gas laminar theory of Stollery & Bates (1974) deteriorates. As Stolley & Bates indicate, this may be due to the assumption in the theory of isentropic flow at the edge of the boundary layer, which is not valid through shocks. One would expect that the theory will yield a less accurate description of the flow as the corner angle is increased. That there is even reasonable agreement between experiment and theory is remarkable, and is the impetus to extend the theory to real gas flows in §4 in order to examine the potential upper limits of any real gas effect on this type of flow.

The possible real gas effects on separation and reattachment of the boundary layer will now be examined. First, as the separation condition is approached, the flow may be examined in terms of the pressure coefficient at separation and the incipient separation angle. The upstream influence and the plateau pressure coefficient, which are also useful means of examining separation, have been dealt with else-
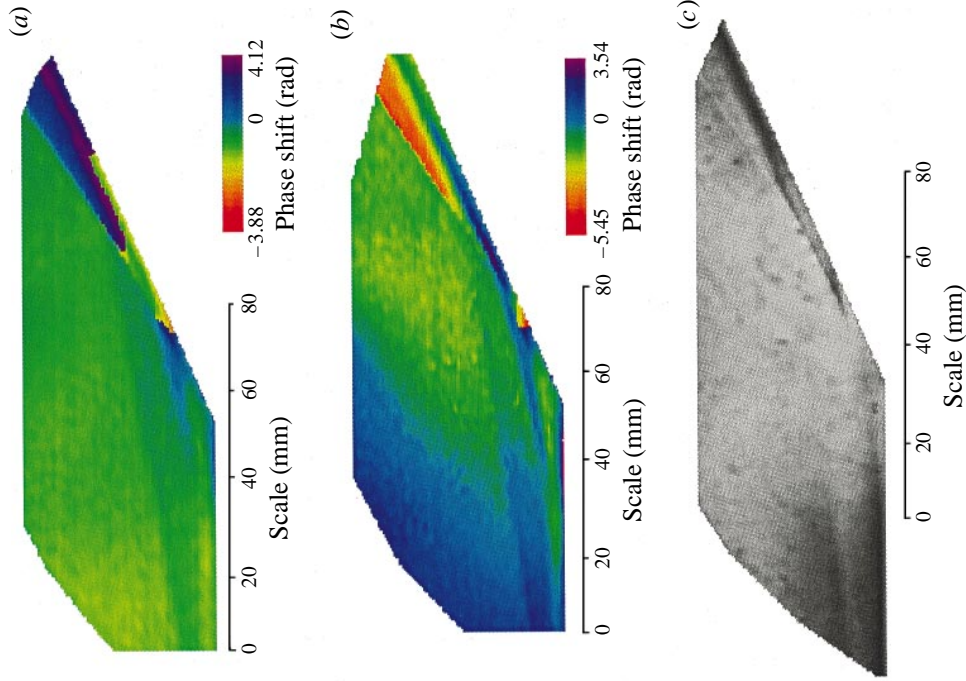
FIGURE 21. Flow visualization for $\theta_w = 24°$: (*a*) condition B; (*b*) condition D; (*c*) condition B (infinite fringe).
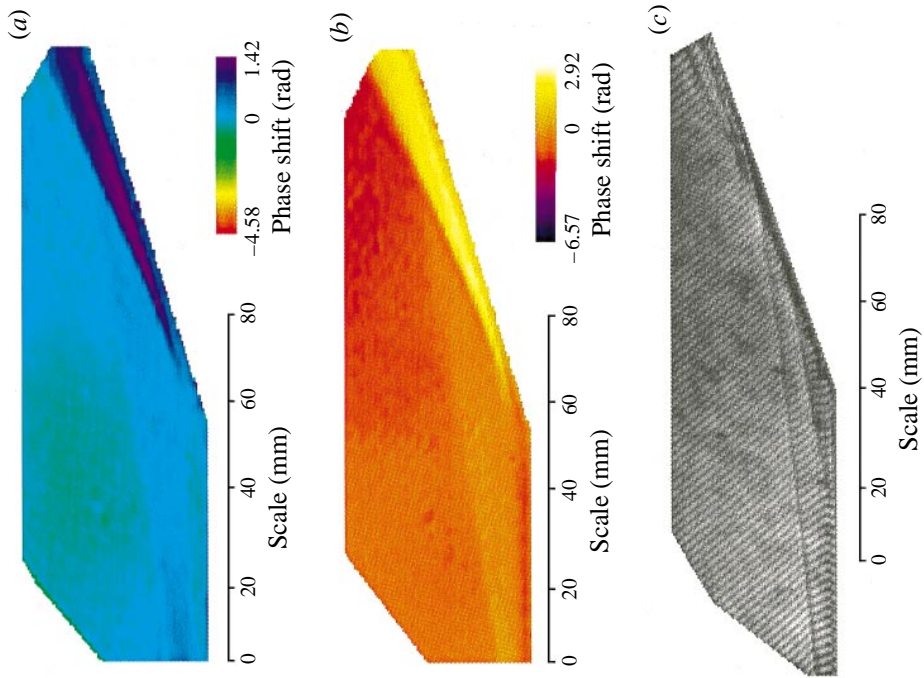

FIGURE 18. Flow visualization for $\theta_w = 18°$: (*a*) condition B; (*b*) condition D; (*c*) condition G.
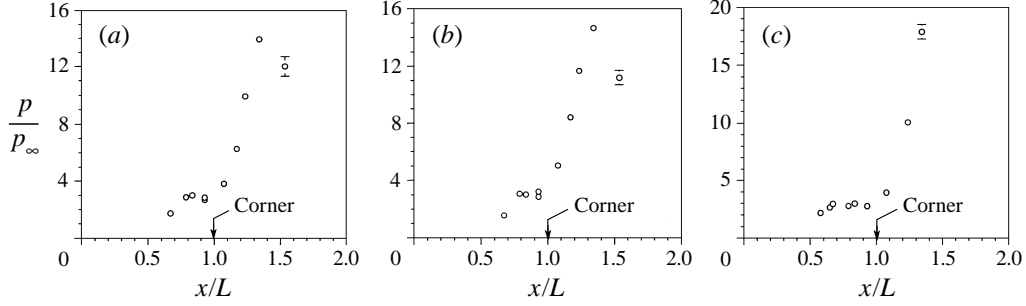
FIGURE 19. Compression corner pressure distributions, $\theta_w = 24°$. (*a*) condition B; (*b*) condition D; (*c*) condition G. Refer to figure 8 for explanation of symbols.
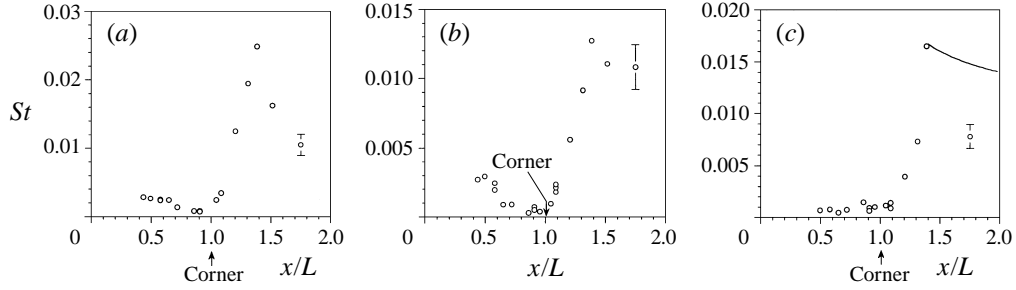

FIGURE 20. Compression corner heat transfer distributions, $\theta_w = 24°$. (*a*) condition B; (*b*) condition D; (*c*) condition G. ◯, experimental data; —— Stollery & Bates (1974) turbulent theory.

where (Mallinson 1994; Mallinson *et al.* 1996*a*). Next, the relationship between peak heating and peak pressure gives some idea of the flow behaviour near reattachment.

The free interaction concept of Chapman *et al.* (1958) postulates that separation is independent of the agency which provokes it and that it depends upon the Mach and Reynolds number upstream of the interaction. Thus, the pressure rise to separation does not depend directly upon the corner angle. Of course, the upstream separation location will depend upon the corner angle (Délery 1989) and so this will affect the local values of Mach and Reynolds numbers. For laminar flow, the pressure coefficient at separation, $C_{p,s}$, has been found to be of the form (Gadd 1957; Chapman *et al.* 1958; Hakkinen *et al.* 1959; Curle 1961; Erdos & Pallone 1962)

$$C_{p,s} \equiv \frac{p_s - p_\infty}{\frac{1}{2}\rho_\infty U_\infty^2} = k\left\{Re_{x_o}\left(M_o^2 - 1\right)\right\}^{-1/4} \qquad (3.10)$$

where p_s is the pressure at separation, k is a constant of proportionality and the subscript '*o*' refers to conditions evaluated just upstream of the interaction at x_o (see figure 1). The values of the constant of proportionality found by the various investigators are: 1.13 (Gadd), 0.93 (Chapman *et al.*), 1.15 (Hakkinen *et al.*), 0.83 (Curle) and 1.03 (Erdos & Pallone). Note that the Curle value was obtained from a Polhausen-type analysis which is known to be unsatisfactory for separated flows and so will not be compared with experimental data here.

The separation pressure coefficient data from the present experiments are compared in terms of the Mach–Reynolds parameter of (3.10) in figure 22. Also shown are values from the above-mentioned theories and experimental data from the low-enthalpy experiments of Chapman *et al.* (1958), Lewis *et al.* (1968), Holden &
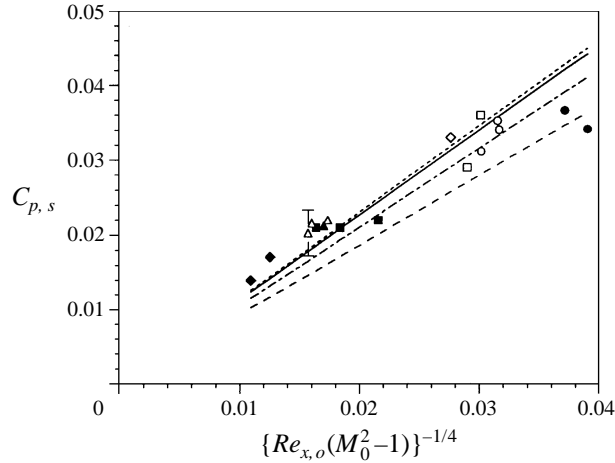
FIGURE 22. Separation pressure coefficient for low- and high-enthalpy flows. Symbols represent experimental data, curves represent theory. O, □, △, conditions B, D and G, respectively, present experiments; ◇, Rayner (1973); ●, Chapman *et al.* (1958); ■, Lewis *et al.* (1968); ▲, Holden & Moselle (1970); ◊, Kumar & Stollery (1994); ———, Gadd (1957); – – – –, Chapman *et al.* (1958); - - - -, Hakkinen *et al.* (1959); – · – · –, Erdos & Pallone (1962).

Moselle (1970) and Kumar & Stollery (1994) and the high-enthalpy experiments of Rayner (1973). Note that the results from the Rayner study for flows with total enthalpy $h_0 \geqslant 25$ MJ kg^{-1} have been omitted here as these flows are now believed to suffer from driver gas contamination. The error bar represents $\pm 15\%$ which is indicative of the scatter. It is seen that the separation pressure data for both high- and low-enthalpy flows are correlated reasonably well in this form considering the large variation in experimental conditions. The Chapman *et al.* (1958) data are seen to lie about 10% below the other data. The reason for this is unclear.

For perfect gas flows, the incipient separation angle, θ_i, is given by (Needham 1967; Hankey 1967; Inger 1994)

$$M_\infty \theta_i \approx 1.3 \bar{\chi}_L^{1/2} \tag{3.11}$$

where $\bar{\chi}_L$ is the value of $\bar{\chi}$ evaluated at the corner, $x = L$, and θ_i is in radians. The incipient separation angle for conditions B, D and G, as estimated from the pressure and heat transfer distributions and the flow visualization data, is shown in table 2 along with predictions from (3.11). The experimental values compare fairly well with the theoretical predictions.

The 4° uncertainty band about the experimental value of incipient separation angle for the condition G flow has been estimated in the following way. In conditions B and D flows with corner angles beyond 1° either side of θ_i, the data show evidence of being separated or attached. There is no reason to expect the transition in condition G flow from attached to separated would occur over a wider band of corner angles than for condition B and D flows. The 5° and 15° corner angle condition G flows are clearly attached and clearly separated, respectively. This indicates that the incipient separation angle is somewhat removed from both these values. The 10° corner angle condition G flow exhibits features which could be argued to be consistent with incipient separation, although the large scatter in the heat transfer data and the absence of data for corner angles immediately above and below 10°, in which a trend might have been observed, mean that a claim of $\theta_i = 10^o$ cannot be made with the

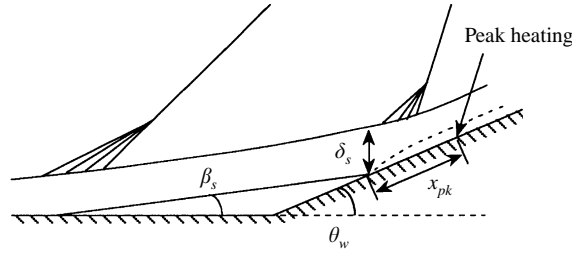| Condition	$\bar{\chi}_L$	θ_i(deg.) Experiment	θ_i(deg.) Theory, (3.11)
B	2.28	15 ± 1	14.9
D	1.97	15 ± 1	13.9
G	1.24	10 ± 2	9.0

TABLE 2. Incipient separation angle.

FIGURE 23. Scale of reattaching boundary layer in compression corner flow
(after Bushnell & Weinstein 1968).

degree of certainty associated with the claims for the condition B and D values of θ_i. On balance, therefore, it is most likely that the value of θ_i for condition G lies between $8°$ and $12°$, that is, $10° \pm 2°$.

It would therefore seem, from figure 22 and table 2, that for the present high-enthalpy flow conditions, the real gas effects on separation are small. A similar conclusion was been reached elsewhere based on the upstream influence and plateau pressure data (Mallinson 1994; Mallinson et al. 1996a).

The relationship between the peak heating, q_{pk}, and the peak pressure, p_{pk}, near reattachment has been shown by Neumann (1972) and Holden (1975, see Hankey & Holden 1975) to be of the form

$$\frac{q_{pk}}{q_{fp}} = \left(\frac{p_{pk}}{p_{fp}} \right)^n \qquad (3.12)$$

where $n = 0.7$ for laminar flows and $n = 0.85$ for turbulent flows. The subscript fp refers to the flat-plate value at the location corresponding to the peak value.

Simeonides et al. (1994) recognized that for separated flows, the growth length scale of the reattaching boundary layer, L_{pk}, plays an important role in determining the level of peak heating for separated flows. The peak heating for separated flows was shown to be given by

$$\frac{q_{pk}}{q_{fp}} = \left(\frac{p_{pk}}{p_{fp}} \right)^{1-m} \left(\frac{x_{pk}}{L_{pk}} \right)^m \qquad (3.13)$$

where $m = 0.5$ for laminar flow, $m = 0.2$ for turbulent flow and x_{pk} is the distance from the model leading edge to the location of peak heating (see figure 23).

The experimental peak pressure and peak heat transfer ratios from the present study are presented in table 3. The heat transfer ratio is presented in terms of the Stanton numbers to account for the slight shot-to-shot variations in the free-stream conditions. The uncertainties in the experimental values for the peak to flat-plate ratios arise from the accumulation of the uncertainties in the respective flat-plate and

Condition	θ_w(deg.)	p_{pk}/p_{fp} Experiment $\pm14\%$	St_{pk}/St_{fp} Experiment $\pm20\%$	St_{pk}/St_{fp} Theory, (3.12)	St_{pk}/St_{fp} Theory, (3.13)
B	10	3.8	2.2	2.5	–
	15	5.5	3.5	3.3	–
	18	7.3	4.9	4.0	6.5
	24	12.4	13.2	5.8	12.5
D	10	3.7	2.8	2.5	–
	15	6.4	3.4	3.7	–
	18	7.3	4.9	4.0	6.2
	24	12.4	7.8	5.8	8.4
G	10	3.7	2.5	2.5	–
	15	8.6	16.2	4.5	15.2
	18	12.2	23.6	5.8	18.0
	24	16.6	29.9	7.1	–

TABLE 3. Peak heating–peak pressure variation. The dashes indicate either that the flow is attached and so (3.13) is not applicable to that flow condition or that no data are available.

peak values. Also shown are the values from the laminar form of the Neumann–Holden correlation (3.12) and the laminar Simeonides *et al.* (1994) expression for separated flows, (3.13). When using the latter, the value of L_{pk} was taken as given by Bushnell & Weinstein (1968):

$$L_{pk} = \frac{\delta_s}{\sin(\theta_w - \beta_s)} \tag{3.14}$$

with the values for the shear layer thickness at reattachment, δ_s, and the angle of the separating shear layer, β_s, obtained from interferograms where available.

The Neumann–Holden relation compares reasonably well with the results for small corner angles where the flow is attached or has a small separated region. For larger corner angles, where the flow is well separated, the comparison between this theory and the experimental data is poor. The method of Simeonides *et al.* (1994) appears, however, to be in reasonable agreement with the data for the well separated flows.

It would therefore seem that there is little difference between the peak heating–peak pressure relationship for the high- and low-enthalpy flows. That is, the real gas effects do not have an significant impact on the compression corner flows for the present conditions.

4. Hypersonic viscous interaction of an equilibrium dissociating gas

4.1. *Hypersonic viscous interaction model*

The concept of local flat-plate similarity was employed by Cheng *et al.* (1961) to model the flow over flat plates at positive, zero and negative incidence. The growth of the boundary layer was assumed to determine an effective body shape and the pressure was obtained from local inclination methods. The boundary layer displacement thickness was assumed to be a function of the pressure distribution and, thus, a solution could be obtained by iteration.

Stollery (1970) demonstrated that the local flat-plate similarity method could be applied to compression corner flow. Good agreement was achieved between theory and experimental data provided the flows were attached or had only a small separated region. It should be noted that that the model is strictly applicable to attached flows

only. Thus, the rounded minimum in heat transfer and plateau in pressure that are observed experimentally in separated flows (Délery 1989) are not predicted by the hypersonic viscous interaction model.

In a later paper that concentrated mainly on turbulent boundary layers, Stollery & Bates (1974) derived a new function describing the boundary layer displacement thickness for laminar flows which was similar to the expression used by Cheng *et al.* (1961) and Stollery (1970). Calculations performed using the Stollery & Bates laminar expression have subsequently been found to compare well with experimental data for flat-plate and compression corner flow of a perfect gas (Mallinson 1994).

It was found in §3 that although the enthalpies of the current experiments were moderate to high, the compression corner flow did not exhibit any significant sensitivity to real gas effects under the conditions tested. It is, however, still of interest to investigate the effects of real gas behaviour on shock wave/boundary layer interaction. The Stollery & Bates (1974) viscous interaction model will be extended, in this section, to include equilibrium real gas effects. This new model will then be employed in §5 to determine possible upper limits of the real gas effects.

4.2. *Equilibrium dissociating gas model*

The present model for the gas chemistry is based on the Lighthill (1957) ideal dissociating gas (IDG). In that formulation, the equilibrium dissociation fraction, α, is given by

$$\frac{\alpha^2}{1-\alpha} = \frac{\exp\left(-\theta_d/T\right)}{\rho} \left[m\left(\frac{\pi m \mathrm{k}}{\mathrm{h}^2}\right)^{3/2} \theta_r T^{1/2} \left\{1 - \exp\left(-\theta_v/T\right)\right\} \frac{\left(Q_{el}^a\right)^2}{Q_{el}^{aa}} \right] \qquad (4.1)$$

where θ_r, θ_v and θ_d are the characteristic temperatures for rotation, vibration and dissociation, respectively, m is the mass of the atomic species, k is Boltzmann's constant, h is Planck's constant and Q_{el}^a and Q_{el}^{aa} are the electronic partition functions for the atom and molecule, respectively. For simplicity, nitrogen will be assumed as the test gas in the theoretical part of this study. Values for the characteristic temperatures are given by Vincenti & Kruger (1965) for nitrogen as: $\theta_r = 2.9$ K, $\theta_v = 3390$ K, and $\theta_d = 113000$ K.

Lighthill (1957) found that for nitrogen the term inside the square brackets was nearly constant for temperatures in the range 1000–7000 K and therefore made the approximation that this factor is constant. The maximum temperature within the boundary layer may be up to 8000 K in the present study and so, to preserve generality, the factor inside the square brackets will not be taken as constant here. The partition functions for electronic excitation of atomic and molecular nitrogen are, however, almost independent of temperature up to approximately 10000 K (see Vincenti & Kruger 1965, §IV.11 and IV.12) and may be taken as constant. Thus, the present model differs from the IDG by not assuming the factor in the square brackets to be constant.

The enthalpy and pressure for the present model are the same as for the IDG model and are given by (Lighthill 1957)

$$h = RT \left\{ \frac{7 + 3\alpha}{2} + \frac{(1-\alpha)\,\theta_v/T}{\exp\left(\theta_v/T\right) - 1} + \frac{\alpha\theta_d}{T} \right\} \qquad (4.2)$$

and

$$p = (1 + \alpha)\,\rho RT \qquad (4.3)$$

respectively. For nitrogen, R has a constant value of 296.9 J kg^{-1} K^{-1}.

Condition	M_∞	Re_∞ $(\times 10^{-5}\ \mathrm{m}^{-1})$	γ_∞	T_w (K)	T_w/T_0	T_∞ (K)
1	10.0	5.13	1.4	300	0.014	1000
2	6.9	5.10	1.4	300	0.019	1500
3	7.7	2.63	1.4	1000	0.111	700

TABLE 4. Flow conditions for theoretical study.
Note that T_0 is calculated assuming frozen chemistry.

4.3. *Flow conditions and geometry*

Three test flow conditions were chosen to demonstrate the real gas effects: (1) a generic free-piston shock tunnel condition; (2) a test condition for the GASL Hypulse expansion tube (Hackett 1993); and (3) a re-entry flight path condition at an altitude of 54.8 km taken from the early flights of the space shuttle orbiter (Gnoffo, Weilmuenster & Alter 1994). As stated earlier, nitrogen will be taken as the test gas. For the conditions chosen, the free stream is undissociated.

It is not expected that in practical situations equilibrium conditions would prevail throughout the complete flow field for any of these conditions. The conditions were chosen as they gave a range of Mach and Reynolds numbers and wall-to-total temperature ratios that are of practical importance. However, considering equilibrium flow allows an upper bound to be determined for the real gas effects at these flow conditions.

The geometry is a 0.5 m flat plate to which is attached a 0.5 m ramp plate. For the present study, calculations have been performed for ramp angles of 5°, 7.5° and 10°. The plate was set at an angle of incidence of $+10°$ for condition 3, to simulate a re-entry configuration of a forebody plus flap. The inviscid flow behind the leading-edge shock was assumed frozen for this condition. The important flow variables for the three conditions are shown in table 4. For condition 3, the conditions are those behind the leading-edge shock.

4.4. *Real gas effects on the boundary layer*

It is assumed that the boundary layer temperature profiles are given by the Crocco integral (Stewartson 1964)

$$\frac{T}{T_e} = \frac{T_w}{T_e}(1 - f') + f' + Pr^{1/2}\left(\frac{\gamma - 1}{2}\right)M_e^2 f'(1 - f') \tag{4.4}$$

and the velocity profile, f', is given by the Blasius solution. For the equilibrium gas, it was assumed that the enthalpy equalled that for the perfect gas. Using (4.1) and (4.2), the equilibrium temperature was found by iteration. The resulting profile is related to the physical plane via the Howarth–Dorodnitsyn transformation.

The perfect gas and equilibrium dissociating gas flat-plate boundary layer temperature profiles for conditions 1, 2 and 3 are shown in figure 24(*a*–*c*), respectively. Note the reduction in both the thermal boundary layer thickness and the maximum temperature in the boundary layer for the equilibrium case. Although the maximum value of the dissociation fraction, α, is approximately 0.01, the temperature difference between perfect gas and equilibrium gas flows is quite significant, of order 10%. This is because of contributions from both vibrational and dissociational processes.
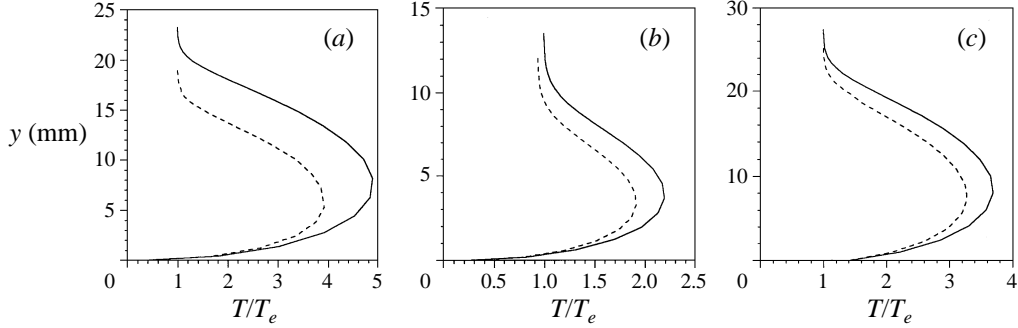
FIGURE 24. Temperature profiles for flat-plate boundary layer flow of an equilibrium dissociating gas: (*a*) condition 1; (*b*) condition 2; (*c*) condition 3. ——, perfect gas theory; – – – –, equilibrium dissociating gas theory.

4.5. *Boundary layer properties*

The boundary layer displacement thickness, δ^*, is given by Stewartson (1964) as

$$\delta^* = \int_0^\infty \left(1 - \frac{\rho}{\rho_e}\frac{u}{u_e}\right)\mathrm{d}y \qquad (4.5)$$

where y is the distance normal to the surface. Using the Howarth–Dorodnitsyn similarity transformation, (4.5) may be rearranged as

$$\frac{\delta^*}{x} = \left(\frac{2}{Re_x}\right)^{1/2}\int_0^\infty \frac{\rho_e}{\rho}\left(1 - \frac{\rho}{\rho_e}\frac{u}{u_e}\right)\mathrm{d}\eta. \qquad (4.6)$$

The enthalpy for the equilibrium dissociating gas, h_{eq}, is equal to the perfect gas value, h_{pg}, and is given by

$$h_{pg} = c_p T_{pg} = h_{eq} = c_p T_{eq} + \Delta E \qquad (4.7)$$

where ΔE is the change in energy due to the presence of vibrational and dissociational equilibrium, T_{eq} is the temperature for an equilibrium dissociating gas and T_{pg} is the temperature that would exist for a perfect gas. Further, it is assumed that $\Delta E > 0$, that is, the overall effect is endothermic. Rearranging (4.7) gives

$$T_{eq} = T_{pg} - \Delta E/c_p \qquad (4.8)$$

where it has been assumed that the difference between the equilibrium and perfect gas values of c_p is small. For temperatures less than approximately 1000 K, this assumption is valid only when the difference between T_{eq} and T_{pg} is small (Gupta *et al.* 1990). For temperatures in the range $1000 \leqslant T \leqslant 8000$ K, the value of c_p is almost constant (Gupta *et al.* 1990) and so the assumption of constant c_p is valid even when large differences between T_{eq} and T_{pg} occur. An examination of the boundary layer temperature profiles in §4.4 reveals that the assumption of constant c_p is reasonable for the present theoretical study.

For an equilibrium dissociating gas, the density profile across the boundary layer is therefore given by

$$\left(\frac{\rho}{\rho_e}\right)_{eq} = \frac{T_e}{T_{pg} - \Delta E/c_p} \qquad (4.9)$$

where it is assumed that the pressure is constant and the value of $(1+\alpha_e)/(1+\alpha) \approx 1$ across the boundary layer. The latter assumption is reasonable given that the

maximum value of α is approximately 0.01 in the present study. In terms of the perfect gas density ratio, therefore, (4.9) becomes

$$\left(\frac{\rho}{\rho_e}\right)_{eq} = \left\{\left(\frac{\rho_e}{\rho}\right)_{pg} - \frac{\Delta E}{c_p T_e}\right\}^{-1}. \tag{4.10}$$

An examination of the profiles presented in §4.4 would seem to indicate that the energy differences between the perfect gas and equilibrium dissociating gas flows are significant but much less than the static enthalpy at the edge of the boundary layer, $h_e = c_p T_e$. Equation (4.10) may therefore be expanded as

$$\left(\frac{\rho}{\rho_e}\right)_{eq} = \left(\frac{\rho}{\rho_e}\right)_{pg} + \frac{\Delta E}{c_p T_e}\left(\frac{\rho}{\rho_e}\right)_{pg}^2 + \text{higher-order terms} \tag{4.11}$$

and so

$$\left(\frac{\rho}{\rho_e}\right)_{eq} \approx \left(\frac{\rho}{\rho_e}\right)_{pg}\left\{1 + \frac{\Delta E}{c_p T_e}\left(\frac{\rho}{\rho_e}\right)_{pg}\right\}. \tag{4.12}$$

This approximation will be used in the knowledge that a small error may be introduced.

Upon substituting (4.12) into (4.6), the boundary layer displacement thickness for an equilibrium dissociating gas may be obtained as

$$\begin{aligned}
\frac{\delta_{eq}^*}{x}\left(\frac{Re_x}{2}\right)^{1/2} &= \int_0^\infty \left(\frac{\rho_e}{\rho}\right)_{eq}\left\{1 - \left(\frac{\rho}{\rho_e}\right)_{eq}\frac{u}{u_e}\right\}\mathrm{d}\eta \\
&= \int_0^\infty \left(\frac{\rho_e}{\rho}\right)_{pg}\left\{1 - \left(\frac{\rho}{\rho_e}\right)_{pg}\frac{u}{u_e}\right\}\mathrm{d}\eta \\
&\quad + \int_0^\infty \left(\frac{\rho_e}{\rho}\right)_{pg}^2\left(\frac{\Delta E}{c_p T_e}\right)^2\frac{u}{u_e}\mathrm{d}\eta - \int_0^\infty \left(\frac{\Delta E}{c_p T_e}\right)\mathrm{d}\eta.
\end{aligned} \tag{4.13}$$

The second term on the right-hand side of (4.13) is much smaller than the first and third terms and may therefore be neglected which leaves

$$\frac{\delta_{eq}^*}{x}\left(\frac{Re_x}{2}\right)^{1/2} \approx \frac{\delta_{pg}^*}{x}\left(\frac{Re_x}{2}\right)^{1/2} - \frac{\Delta\delta_E^*}{x}\left(\frac{Re_x}{2}\right)^{1/2} \tag{4.14}$$

where the reduction in the displacement thickness due to endothermic processes, $\Delta\delta_E^*$, is given by

$$\Delta\delta_E^* = x\left(\frac{2}{Re_x}\right)^{1/2}\int_0^\infty \left(\frac{\Delta E}{c_p T_e}\right)\mathrm{d}\eta. \tag{4.15}$$

The displacement thickness for an equilibrium dissociating gas is therefore

$$\delta_{eq}^* \approx \delta_{pg}^* - \Delta\delta_E^*. \tag{4.16}$$

That is, the boundary layer displacement thickness is reduced due to endothermic processes. For a non-reacting gas, $\Delta E = 0$ and thus the perfect gas boundary layer displacement thickness is recovered. Note that the value of $\Delta\delta_E^*$ will vary with distance along the surface, but its proportionality to δ_{pg}^* will remain constant.

The parameter

$$\frac{\Delta\delta_E^*}{\delta_{pg}^*} = \frac{\delta_{pg}^* - \delta_{eq}^*}{\delta_{pg}^*} \qquad (4.17)$$

describes the relative reduction in displacement thickness due to endothermic processes. It also determines the difference between the shape factors for perfect and equilibrium dissociating gas flows, as will be seen later. The value of $\Delta\delta_E^*/\delta_{pg}^*$ may be evaluated by calculating the integral thickness using the boundary layer profiles presented in figure 24(a–c). For conditions 1, 2 and 3, its value is 0.251, 0.203 and 0.108, respectively.

The length of the separated region will vary directly with displacement thickness (Délery 1989). The profiles presented in figure 24 therefore suggest that the length of the separated region would be reduced by real gas effects due to a decrease in displacement thickness. This is consistent with previous theoretical predictions of shock wave/boundary layer interactions (Ballaro & Anderson 1991; Grasso & Leone 1994) and also with the conjecture made by Park (1990) (see p. 250). Grasso & Leone argued, however, that the reduction in separated length was due to a decrease in shock strength arising from real gas effects. The corner angles they considered for their calculations were small, less than 30°. It is likely that the real gas effects on shock strength would have been negligible for such corner angles.

Based on Stewartson (1964), the momentum thickness, θ, may be written as

$$\begin{aligned}
\theta_{eq} &= \int_0^\infty \left(\frac{\rho_e}{\rho}\right)_{eq} \frac{u}{u_e}\left(1 - \frac{u}{u_e}\right)\mathrm{d}y \\
&= x\left(\frac{2}{Re_x}\right)^{1/2}\int_0^\infty \frac{u}{u_e}\left(1 - \frac{u}{u_e}\right)\mathrm{d}\eta \\
&= \theta_{pg}.
\end{aligned} \qquad (4.18)$$

That is, the change in density profile which occurs due to endothermic reactions has no effect on the value of momentum thickness. This is because the transformation in the y–variable cancels the density ratio in the expression for momentum thickness.

4.6. *Extension of hypersonic viscous interaction model to flow of an equilibrium dissociating gas*

The flat-plate similarity method relies upon knowledge of the value of the shape factor, H. From the previous section it was found that the displacement thickness is reduced and the momentum thickness is unchanged under the influence of dissociation. The shape factor for an equilibrium dissociating gas is then

$$H_{eq} = \frac{\delta_{eq}^*}{\theta_{eq}} = \frac{\delta_{pg}^* - \Delta\delta_E^*}{\theta_{eq}} = H_{pg}\left(1 - \frac{\Delta\delta_E^*}{\delta_{pg}^*}\right). \qquad (4.19)$$

The shape factor for a perfect gas is given by (Spence 1961; White 1974)

$$H_{pg} \approx \left(\frac{\gamma - 1}{2}\right)M_e^2\left(1 + H_i\frac{T_w}{T_0}\right) \qquad (4.20)$$

where H_i is the incompressible value of the shape factor. For laminar flow, $H_i = 2.6$ (Stollery & Bates 1974). The compressible shape factor for an equilibrium dissociating

gas may therefore be written as

$$H_{eq} \approx \left(\frac{\gamma-1}{2}\right) M_e^2 \left(1 + 2.6\frac{T_w}{T_0}\right)\left(1 - \frac{\Delta\delta_E^*}{\delta_{pg}^*}\right). \tag{4.21}$$

The value for H_{eq} may now be substituted into the momentum integral equation (Stollery & Bates 1974)

$$\frac{\mathrm{d}\theta}{\mathrm{d}x} + \left(H_{eq} + 2 - M_e^2\right)\frac{\theta}{u_e}\frac{\mathrm{d}u_e}{\mathrm{d}x} = \frac{\tau_w}{\rho_e u_e^2}. \tag{4.22}$$

The velocity gradient is given by

$$\frac{1}{u_e}\frac{\mathrm{d}u_e}{\mathrm{d}x} = \frac{1}{M_e}\frac{\mathrm{d}M_e}{\mathrm{d}x}\left\{1 + \left(\frac{\gamma-1}{2}\right)M_e^2\right\}^{-1}. \tag{4.23}$$

Substitution of (4.21) and (4.23) into (4.22) yields

$$\frac{\mathrm{d}\theta}{\mathrm{d}x} + \left\{\left(\frac{\gamma-1}{2}\right)M_e^2\left(1 + 2.6\frac{T_w}{T_0}\right)\left(1 - \frac{\Delta\delta_E^*}{\delta_{pg}^*}\right) + 2 - M_e^2\right\}$$
$$\times \frac{\theta}{M_e}\frac{\mathrm{d}M_e}{\mathrm{d}x}\left\{1 + \left(\frac{\gamma-1}{2}\right)M_e^2\right\}^{-1} = \frac{c_{f_e}}{2}. \tag{4.24}$$

In the hypersonic limit $M_e^2 \gg 1$, so that the inverse of the term inside the second set of curly brackets becomes small and the term inside the first set of curly brackets may be simplified to

$$\left(\frac{\gamma-1}{2}\right)M_e^2\left\{\left(1 + 2.6\frac{T_w}{T_0}\right)\left(1 - \frac{\Delta\delta_E^*}{\delta_{pg}^*}\right) - \frac{2}{\gamma-1}\right\}. \tag{4.25}$$

The momentum equation thus becomes

$$\frac{\mathrm{d}\theta}{\mathrm{d}x} + \left\{\left(1 + 2.6\frac{T_w}{T_0}\right)\left(1 - \frac{\Delta\delta_E^*}{\delta_{pg}^*}\right) - \frac{2}{\gamma-1}\right\}\frac{\theta}{M_e}\frac{\mathrm{d}M_e}{\mathrm{d}x} = \frac{c_{f_e}}{2}. \tag{4.26}$$

For laminar flows, the skin friction coefficient based on the conditions at the edge of the boundary layer is (Stollery & Bates 1974)

$$\frac{c_{f_e}}{2} = \frac{0.221\,C}{M_\infty^3 Re_x/x}\frac{M_e^3}{\theta} = A\frac{M_e^3}{\theta} \tag{4.27}$$

where

$$A = \frac{0.221\,C}{M_\infty^3 Re_x/x} \tag{4.28}$$

The momentum equation, (4.26), can then be re-written as

$$\theta\frac{\mathrm{d}\theta}{\mathrm{d}x} + B\frac{\theta^2}{M_e}\frac{\mathrm{d}M_e}{\mathrm{d}x} = AM_e^3 \tag{4.29}$$

where

$$B = \left(1 + 2.6\frac{T_w}{T_0}\right)\left(1 - \frac{\Delta\delta_E^*}{\delta_{pg}^*}\right) - \frac{2}{\gamma-1}. \tag{4.30}$$

The momentum equation may be integrated to yield

$$\theta = \left(\frac{0.442\,C}{M_\infty^3 Re_x/x} \right)^{1/2} \frac{\left\{ \int_0^x \left(M_\infty/M_e\right)^{-(3+2B)} M_\infty^{3+2B}\,\mathrm{d}\xi \right\}^{1/2}}{\left(M_\infty/M_e\right)^{-B} M_\infty^B} \tag{4.31}$$

where ξ is a dummy variable in x. For isentropic flow in the hypersonic limit, the Mach number ratio may be approximated by

$$\frac{M_e}{M_\infty} \approx \left(\frac{p_e}{p_\infty} \right)^{(1-\gamma)/2\gamma} \tag{4.32}$$

which allows θ to be simplified to

$$\theta = \left(\frac{0.442\,C}{M_\infty^3 Re_x/x} \right)^{1/2} \frac{\left\{ \int_0^x P^{(3+2B)(1-\gamma)/2\gamma}\,\mathrm{d}\xi \right\}^{1/2}}{P^{B(1-\gamma)/2\gamma}} M_\infty^{3/2} \tag{4.33}$$

where P is the pressure ratio, (p_e/p_∞). The displacement thickness may now be written as

$$\frac{M_\infty \delta_{eq}^*}{x} = \frac{M_\infty \theta H_{eq}}{x} = 0.665 \left(\frac{C M_\infty^2}{Re_x/x} \right)^{1/2} \frac{\left\{ \int_0^x P^{(3+2B)(1-\gamma)/2\gamma}\,\mathrm{d}\xi/x \right\}^{1/2}}{P^{B(1-\gamma)/2\gamma}} H_{eq}. \tag{4.34}$$

Substituting (4.21) into (4.34) results in

$$\frac{M_\infty \delta_{eq}^*}{x} = 0.665 \left(\frac{\gamma-1}{2} \right) \left(1 + 2.6\frac{T_w}{T_0} \right) \left(1 - \frac{\Delta\delta_E^*}{\delta_{pg}^*} \right) \bar{\chi} \frac{\left\{ \int_0^x P^{\phi'}\,\mathrm{d}\xi/x \right\}^{1/2}}{P^{\psi'}} \tag{4.35}$$

where

$$\begin{aligned} \phi' &= \frac{(3+2B)(1-\gamma)}{2\gamma} \\ &= \frac{(\gamma-1)}{\gamma} \left\{ \frac{2}{(\gamma-1)} - \frac{3}{2} - \left(1 + 2.6\frac{T_w}{T_0} \right) \left(1 - \frac{\Delta\delta_E^*}{\delta_{pg}^*} \right) \right\} \end{aligned} \tag{4.36}$$

and

$$\begin{aligned} \psi' &= \frac{(2-B)(\gamma-1)}{2\gamma} \\ &= \frac{(\gamma-1)}{\gamma} \left\{ \frac{\gamma}{(\gamma-1)} - \frac{1}{2} \left(1 + 2.6\frac{T_w}{T_0} \right) \left(1 - \frac{\Delta\delta_E^*}{\delta_{pg}^*} \right) \right\}. \end{aligned} \tag{4.37}$$

This expression for the boundary layer displacement thickness of an equilibrium dissociating gas may now be used in conjunction with one of the surface inclination methods to obtain the pressure distribution for flow over a variety of surfaces. Stollery (1970) found the tangent-wedge pressure law:

$$P = 1 + \gamma K \left[\frac{\gamma+1}{4} + \left\{ \left(\frac{\gamma+1}{4} \right)^2 + \frac{1}{K^2} \right\}^{1/2} \right] \tag{4.38}$$

to give the most satisfactory results for compression-corner flow. In (4.38), the pressure parameter, K, is given by

$$K = M_\infty \frac{\mathrm{d}y_{eff}}{\mathrm{d}x} \tag{4.39}$$

where the effective body shape, y_{eff}, is

$$y_{eff} = y_w + \delta_{eq}^* \tag{4.40}$$

and y_w is the geometric thickness of the body. For a flat plate, $y_w = 0$. The tangent-wedge pressure law has been adopted here.

The local skin friction coefficient distribution may be obtained by combining (4.27) and (4.31) which gives

$$M_\infty^3 \frac{c_{f_e}}{2} = 0.332 \left(\frac{M_\infty}{M_e} \right)^{-(3+B)} \frac{\bar{\chi}}{\left\{ \int_0^x \left(M_\infty/M_e \right)^{-(3+2B)} \mathrm{d}\xi/x \right\}^{1/2}}. \tag{4.41}$$

Then, using the relation (Stollery & Bates, 1974)

$$\frac{\rho_e}{\rho_\infty} \approx \left(\frac{M_\infty}{M_e} \right)^{2/(\gamma-1)} \approx P^{1/\gamma} \tag{4.42}$$

the skin friction coefficient based upon the free-stream conditions is obtained as

$$M_\infty^3 \frac{c_{f_\infty}}{2} = 0.332 \, \bar{\chi} \, P^{\psi'} \left(\int_0^x P^{\phi'} \, \mathrm{d}\xi/x \right)^{-1/2}. \tag{4.43}$$

The Stanton number may be obtained from Reynolds' analogy,

$$St = \frac{c_f}{2(Pr^*)^{2/3}} \tag{4.44}$$

which yields

$$M_\infty^3 St_\infty = 0.332 \, (Pr^*)^{-2/3} \, \bar{\chi} \, P^{\psi'} \left(\int_0^x P^{\phi'} \frac{\mathrm{d}\xi}{x} \right)^{-1/2}. \tag{4.45}$$

5. Theoretical considerations of hypervelocity compression-corner flow

5.1. *Real gas effects on pressure and heat transfer distributions*

The pressure distributions for the compression-corner flow of an equilibrium dissociating gas at conditions 1, 2 and 3 are compared with the perfect gas result in figure 25(a–c), respectively. For the flat plate ($\theta_w = 0°$) the pressure for the equilibrium dissociating gas lies slightly below that for a perfect gas. For both perfect and equilibrium gases, the flat-plate pressure will tend towards a common limit because $P \to 1$ as $\mathrm{d}\delta^*/\mathrm{d}x \to 0$, regardless of whether the gas is non-reacting (perfect) or reacting. For the compression corner ($\theta_w > 0°$), the pressure distributions for the equilibrium gas flows indicate a more rapid rise to the maximum value on the ramp, with the maximum value being somewhat lower than that for the perfect gas flows. The differences in the maximum levels are of the same order as those observed on the flat plate.

The Stanton number distributions for the compression-corner flow of an equilibrium dissociating gas at conditions 1, 2 and 3 are compared with the perfect gas result in figure 26(a–c), respectively. For the flat plate ($\theta_w = 0°$), the heat transfer for the

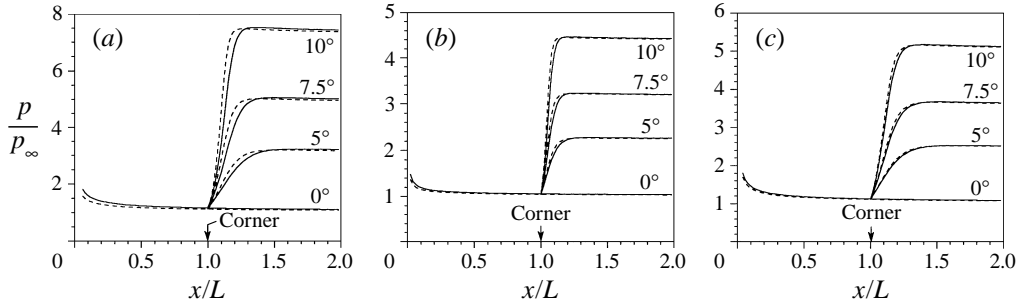FIGURE 25. Theoretical pressure distributions for compression-corner ($L = 0.5$ m). (*a*) condition 1; (*b*) condition 2; (*c*) condition 3. ——, Stollery & Bates (1974) perfect gas theory; $----$, present equilibrium dissociating gas theory.
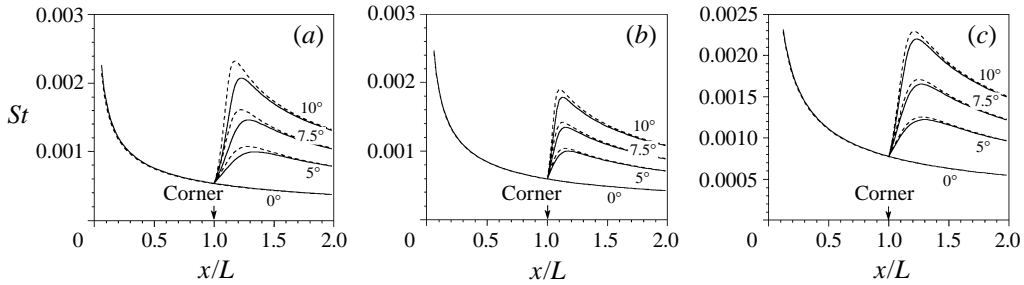

FIGURE 26. Theoretical heat transfer distributions for compression-corner ($L = 0.5$ m): (*a*) condition 1; (*b*) condition 2; (*c*) condition 3. ——, Stollery & Bates (1974) perfect gas theory; $----$, present equilibrium dissociating gas theory.

equilibrium dissociating gas is almost identical to that for the perfect gas. Referring to (4.45), it can be seen that the small difference occurs because the real gas effects on the pressure and on the pressure exponents, ϕ' and ψ', tend to compensate. For the compression corner ($\theta_w > 0°$), it is seen that, as with the pressure distributions, the Stanton number distributions indicate a more rapid rise to the maximum value on the ramp for the equilibrium dissociating gas flow. The heat transfer levels on the face of the ramp are, however, greater for the equilibrium dissociating gas. The greater heat transfer corresponds to the thinner boundary layer near reattachment. This last point is examined further in §5.2.

5.2. *Real gas effects on peak heat transfer*

The variation of peak heat transfer with peak pressure is presented in figure 27 for conditions 1, 2 and 3. Also shown is the prediction from the laminar Neumann–Holden correlation, (3.12). It is evident from this figure that for a given peak pressure level, the heat transfer is greater for the equilibrium dissociating gas model than for a perfect gas flow, the difference increasing with increasing peak pressure level. It is also clear that the variation of peak heat transfer with peak pressure deviates increasingly from the simple Neumann–Holden correlation as the peak pressure ratio increases. The boundary layer thickness, and thus the length scale of the flow near the pressure and heat transfer maxima, L_{pk}, will decrease with increasing peak pressure (Simeonides *et al.* 1994). This reduction in L_{pk} would increase the peak heat transfer levels (see (3.13)).
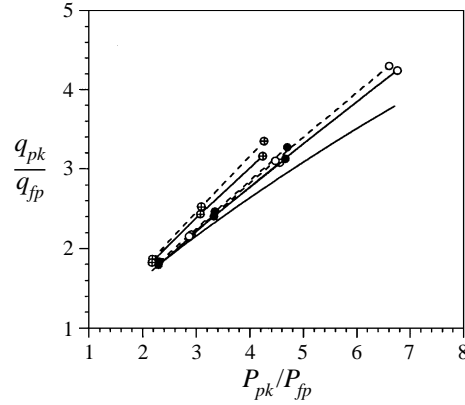
FIGURE 27. Variation of peak heat transfer with peak pressure for perfect and equilibrium dissociating gases: —○—, condition 1, perfect; − − ○ − −, condition 1, equilibrium; —⊕—, condition 2, perfect; − − ⊕ − −, condition 2, equilibrium; —●—, condition 3, perfect; − − ● − −, condition 3, equilibrium.

Consider the product of peak heat transfer and boundary layer displacement thickness at the location of peak heating. The ratio of this product for equilibrium dissociating gas and perfect gas flows is

$$
\frac{\left(q_{pk}\delta_{pk}^*\right)_{eq}}{\left(q_{pk}\delta_{pk}^*\right)_{pg}} = \frac{\left\{\dfrac{\bar{\chi}P^{\psi'}}{\left(\int_0^{x_{pk}} P^{\phi'}\mathrm{d}\xi/x\right)^{1/2}}\left(1 - \dfrac{\Delta\delta_E^*}{\delta_{pg}^*}\right)\bar{\chi}\dfrac{\left(\int_0^{x_{pk}} P^{\phi'}\mathrm{d}\xi/x\right)^{1/2}}{\bar{\chi}P^{\psi'}}\right\}_{eq}}{\left\{\dfrac{\bar{\chi}P^{\psi'}}{\left(\int_0^{x_{pk}} P^{\phi'}\mathrm{d}\xi/x\right)^{1/2}}\bar{\chi}\dfrac{\left(\int_0^{x_{pk}} P^{\phi'}\mathrm{d}\xi/x\right)^{1/2}}{\bar{\chi}P^{\psi'}}\right\}_{pg}} = \left(1 - \frac{\Delta\delta_E^*}{\delta_{pg}^*}\right).
$$

(5.1)

The ratio on the left-hand side of (5.1) has been calculated for conditions 1, 2 and 3 at the three angles considered and is presented in figure 28. The factor is constant for each condition at all corner angles and is consistent with the values of of $\Delta\delta_E^*/\delta_{pg}^*$ obtained in §4.4.

This suggests that the greater the reduction in boundary layer displacement thickness due to endothermic processes, the greater the increases in heat transfer over perfect gas levels near reattachment.

6. Summary and conclusions

The shock wave/boundary layer interaction at a compression corner has been examined both experimentally and theoretically under high-enthalpy reacting flow conditions.

For the datum case of flat-plate flow, the experimental pressure data were found to compare well with the flat-plate similarity theory of Stollery & Bates (1974) which was derived for perfect gas flows. The data also compared well with other experimental data obtained under low-to-moderate enthalpy conditions. The heat transfer data
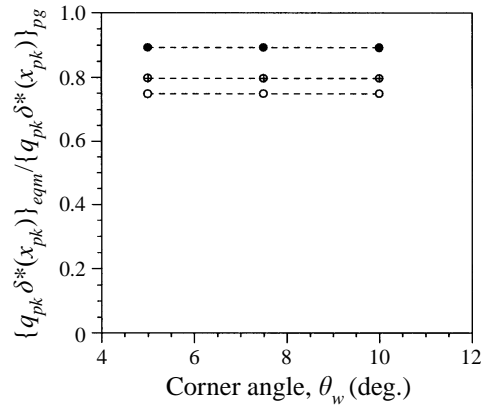
FIGURE 28. Variation of heat transfer–displacement thickness factor, (5.1), with corner angle.
$- - \bigcirc - -$, condition 1; $- - \oplus - -$, condition 2; $- - \bullet - -$, condition 3.

were seen to compare well with the reference enthalpy method (Eckert 1955) and the Stollery & Bates (1974) laminar viscous interaction theory, both modified to include the effects of dissociated species in the free stream (East *et al.* 1980), and also with other experimental data obtained under low-to-moderate enthalpy conditions. An examination of the reaction rates in the boundary layer and external flow showed that the flow is essentially chemically frozen.

It is therefore concluded that the real gas effects on pressure and heat transfer for the flat plate are negligible for the present experimental conditions.

For the compression corner flow, the experimental heat transfer distributions were seen to compare well with the laminar perfect gas theory of Stollery & Bates (1974), modified to include the effects of dissociated species in the free stream, when the flow was attached and just past separation. The comparison with the pressure distributions was only fair.

The experimental data for the separation pressure coefficient, the incipient separation angle and the peak heating near reattachment were found to compare well with experimental data at low enthalpies and theories derived for perfect gas flows.

It is therefore concluded that the real gas effects on the compression corner flow are also negligible for the present experimental conditions.

It was shown that the Stollery & Bates (1974) flat-plate similarity theory can be extended to include equilibrium real gas effects using a generalized Lighthill (1957) ideal dissociating gas model.

This extended model predicts the flat-plate pressure to be slightly lower for the equilibrium flow than that for the perfect gas flow, whilst the heat transfer seems hardly affected. This is consistent with the present experimental observations.

For the compression corner, the new theory predicts a more rapid rise to the maximum pressure and heat transfer on the face of the ramp compared to perfect gas theory. The peak pressure was found to be slightly lower and the peak heat transfer to be slightly higher for the real gas flows. The increase in peak heat transfer over perfect gas levels was shown to correlate well with the reduction in displacement thickness due to real gas effects in the boundary layer.

ulties, Australian National University for advice and assistance with the experiments and Dr. D. J. Bone of the Division of Information Technology, CSIRO, Canberra for permission to use the interferogram analysis software. The flow visualization data were prepared for presentation using the public domain software NIH Image v1.49.

REFERENCES

AMICK, J. L. 1959 *J. Aerospace Sci.* **26**, 603–604.

ANDERSON, J. D. 1989 *Hypersonic and High Temperature Gas Dynamics.* McGraw-Hill.

ANDERS, J. B. 1970 *NASA Tech. Note* D–5791.

ANDERS, J. B. & EDWARDS, C. L. W. 1968 *NASA Tech. Note* D–4320.

BALL, K. O. W. 1971 *AIAA J.* **9**, 2080–2081.

BALL, K. O. W. & KORKEGI, R. H. 1968 *AIAA J.* **6**, 239–243.

BALLARO, C. A. & ANDERSON, J. D. 1991 *AIAA Paper* 91-0250.

BLOY, A. W. & GEORGEFF, M. P. 1974 *J. Fluid Mech.* **63**, 431–447.

BONE, D. J., BACHOR, H.-A. & SANDEMAN, R. J. 1986 *Appl. Optics* **25**, 1653–1660.

BOYCE, R. R., MORTON, J. W., HOUWING, A. F. P., MUNDT, CH. & BONE, D. J. 1994 *AIAA Paper* 94-0282.

BOYCE, R. R. & MUNDT, CH. 1991 *Proc. 1991 Intl Aerosp. Conf. Melbourne, Australia*, Vol. 3, 23-31.

BUSHNELL, D. M. & WEINSTEIN, L. M. 1968 *J. Spacecraft & Rockets* **5**, 1111–1112.

CAPIAUX, R. & WASHINGTON, M. 1963 *AIAA J.* **1**, 650–660.

CARTER, J. E. 1972 *NASA Tech. Rep.* R-385.

CHAPMAN, D. R., KUEHN, D. M. & LARSON, H. K. 1958 *NACA Rep.* 1356.

CHENG, H. K., HALL, J. G., GOLIAN, T. C. & HERTZBERG, A. 1961 *J. Aerospace Sci.* **28**, 353–381, 410.

CRANE, K. C. A. & STALKER, R. J. 1977 *J. Phys.* D: *Appl. Phys.* **10**, 679–695.

CURLE, L. 1961 *Aero. Q.* **12**, 309–336.

DÉLERY, J. 1989 *AGARD Rep.* 761, Pt 9.

DUMITRESCU, L. Z. & PREDA, S. 1985 *Proc. Fifteenth Intl Symp. on Shock Waves & Shock Tubes*, pp. 503–507. Stanford University Press.

EAST, R. A., STALKER, R. J. & BAIRD, J. P. 1980 *J. Fluid Mech.* **97**, 673–699.

ECKERT, E. R. G. 1955 *J. Aero. Sci.* **22**, 585–587.

EDNEY, B. 1968 *Aeronautical Research Institute of Sweden, FFA Rep.* 115.

ERDOS, J. & PALLONE, A. 1962 *Proc. Heat Transfer & Fluid Mechanics Inst.*, Vol. 15, pp. 239–254. Stanford University Press.

FAY, J. F. & SAMBAMURTHI, J. 1992 *AIAA Paper* 92-2896.

GADD, G. E. 1956 *J. Aero. Sci.* **23**, 225–230.

GADD, G. E. 1957 *J. Aero. Sci.* **24**, 759–771, 784.

GAI, S. L. & JOE, W. S. 1992 *J. Thermophys. Heat Transfer* **6**, 433–438.

GAI, S. L., MUDFORD, N. R. 1992 *Shock Waves* **2**, 43–47.

GAI, S. L., MUDFORD, N. R. & HACKETT, C. 1992 *AIAA Paper* 92-3907.

GAI, S. L., REYNOLDS, N. T., ROSS, C. & BAIRD, J. P. 1989 *J. Fluid Mech.* **199**, 541–561.

GNOFFO, P. A., WEILMUENSTER, K. J. & ALTER, S. J. 1994 *J. Spacecraft Rockets* **31**, 367–377.

GRASSO, F. & LEONE, G. 1994 *Proc. IUTAM Symp. Aerothermochemistry of Spacecraft and Associated Hypersonic Flows. Marseille, France*, pp. 220–227. Jouve (Paris).

GRASSO, F., LEONE, G. & DÉLERY, J. M. 1994 *AIAA J.* **32**, 1820–1827.

GRUMET, A., ANDERSON, J. D. & LEWIS, M. J. 1994 *J. Thermophys. Heat Transfer* **8**, pp. 40–47.

GUPTA, R. N. YOS, J. M., THOMPSON, R. A. & LEE, K.-P. 1990 *NASA Ref. Pub.* 1232.

HACKETT, C.M. 1993 *AIAA Paper* 93-3135.

HAKKINEN, R. J., GREBER, I., TRILLING, L. & ABARBANEL, S. S. 1959 *NASA Memo* 2-18-59W.

HAHN, T. O., SHIH, T. I.-P. & CHYU, W. J. 1993 *AIAA J.* **31**, 869–876.

HANKEY, W. L. 1967 *AIAA J.* **5**, 355–356.

HANKEY, W. L. & HOLDEN, M. S. 1975 *AGARDograph* 203.

HANSEN, C. F. 1959 *NASA Tech. Rep.* R-50.

HARVEY, W. D. 1968 *NASA Tech. Note* D-4671.

HE, Y. 1991 Transition and heat transfer in compressible boundary layer flow over a flat plate. PhD Thesis, University of Queensland, Brisbane.

HIRSCHFELDER, J. O., CURTISS, C. F. & BIRD, R. B. 1967 *Molecular Theory of Gases and Liquids*, 4th Edn. Wiley & Sons.

HOLDEN, M. S. 1965 *Cornell Aero. Lab. Rep.* AI-1972-A-3.

HOLDEN, M. S. 1966 *AIAA J.* **4**, 790–799.

HOLDEN, M. S. 1967 *USAF Aerospace Res. Lab. Rep.* 67-0112.

HOLDEN, M. S. 1971a *AIAA J.* **9**, 84–93.

HOLDEN, M. S. 1971b *AIAA J.* **9**, 2296–2298.

HOLDEN, M. S. 1978 *AIAA Paper* 78–1169.

HOLDEN, M. S. & MOSELLE, J. R. 1970 *USAF Aerospace Res. Lab. Rep.* 70-0002.

HUNG, C. M. & MACCORMACK, R. W. 1976 *AIAA J.* **14**, 475–481.

INGER, G. R. 1994 *Aeronaut. J.* **98**, 227–231.

IKAWA, H. 1977 *AIAA J.* **14**, 669–675.

JESSEN, C., VETTER, M. & GRÖNIG, H. 1993 *Flugwiss Weltraumforsch.* **17**, 73–81.

JOHNSON, C. B. 1968 *NASA Tech. Note* D–4308.

KATZER, E. 1989 *J. Fluid Mech.* **206**, 477–496.

KELLY, G. M., SIMMONS, J. M., PAULL, A. 1992 *AIAA J.* **30**, 844–845.

KLINEBERG, J. F. & LEES, L. 1969 *AIAA J.* **7**, 2211–2221.

KUMAR, D. & STOLLERY, J. L. 1993 *Proc. Nineteenth Intl Symp. on Shock Waves, Marseille, France*, Vol. 1, 47–52.

KUMAR, D. & STOLLERY, J. L. 1994 *19th ICAS Congress, ICAS Paper* 94-4. 4. 3.

LEES, L. & REEVES, B. L. 1964 *AIAA J.* **2**, 1907–1920.

LEE, J. Y. & LEWIS, M. J. 1993 *J. Spacecraft Rockets* **30**, 152–163.

LEWIS, J. E., KUBOTA, T. & LEES, L. 1968 *AIAA J.* **6**, 7–14.

LIEPMANN, H. W. & ROSHKO, A. 1957 *Elements of Gasdynamics*. Wiley & Sons.

LIGHTHILL, M. J. 1957 *J. Fluid Mech.* **2**, 1–32.

MADHAVAN, N. S. & SWAMINATHAN, V. 1986 *Intl J. Num. Methods Fluids* **6**, 387–393.

MALLINSON, S. G. 1994 Shock wave/boundary layer interaction at a compression corner in hyper-velocity flows. PhD Thesis, University College (University of New South Wales), Canberra.

MALLINSON, S. G. & GAI, S. L. 1994 *Proc. IUTAM Symp. Aerothermochemistry of Spacecraft and Associated Hypersonic Flows, Marseille, France*, 368–373. Jouve (Paris).

MALLINSON, S. G., GAI, S. L. & MUDFORD, N. R. 1996a *AIAA J.* **34**, 1130–1137.

MALLINSON, S. G., GAI, S. L. & MUDFORD, N. R. 1996b *Aero. J.* **100**, 135–141.

MCINTOSH, M. K. & HORNUNG, H. G. 1970 *AIAA J.* **8**, 1156–1157.

MEE, D. J. & GOYNE, C. G. 1995 *21st Intl Symp. on Shock Waves*, Pasadena, CA, USA.

MILLER, D. S., HIJMAN, R. & CHILDS, M. E. 1964 *AIAA J.* **2**, 312–321.

NEEDHAM, D. A. 1965 *AIAA J.* **3**, 781–783.

NEEDHAM, D. A. 1967 *AIAA J.* **5**, 2284–2285

NEEDHAM, D. A. & STOLLERY, J. L. 1966 *AGARD Conf. Proc.* Vol. 4, Part 1, pp. 89–119.

NEUMANN, R.D. 1972 *AGARD Lecture Series* 42, Vol. 1, Lecture 7.

PARK, C. 1990 *Nonequilibrium Hypersonic Aerothermodynamics*. Wiley.

POWER, G. D. & BARBER, T. J. 1986 *AIAA J.* **26**, 832–840.

PUTNAM, L. E. 1965 *NASA Tech. Note* D-2833.

RAMAKRISHNAN, R., THORNTON, E. A. & WEITING, A. R. 1991 *J. Thermophys. Heat Transfer* **5**, 308–317.

RAYNER, J. P. 1973 Boundary layer separation and thermal choking. PhD Thesis, Australian National University, Canberra.

RIZZETTA, D. & MACH, K. 1989 *AIAA Paper* 89-1877.

RUDY, D. H., THOMAS, J. L., KUMAR, A., GNOFFO, P. A. & CHAKRAVARTHY, S. R. 1991 *AIAA J.* **29**, 1108–1113.

SCHULTZ, D. L. & JONES, T. V. 1973 *AGARDograph* 165.

SIMEONIDES, G., HAASE, W. & MANNA, M. 1994 *AIAA J.* **32**, 301–310.

SPENCE, D. A. 1961 *Aeronaut. Res. Counc. R & M* 3191.

STACEY, C. H. B. 1989 Swept shock wave/boundary layer interactions at high Mach number. PhD Thesis, University of Queensland, Brisbane.

STALKER, R. J. 1972 *Aeronaut. J.* **76**, 374–384.

STALKER, R. J. 1989a *Ann. Rev. Fluid Mech.* **21**, 37–60.

STALKER, R. J. 1989b *AIAA J.* **27**, 1761–1769.

STEWARTSON, K. 1964 *The Theory of Laminar Boundary Layers in Compressible Fluids.* Oxford University Press.

STOLLERY, J. L. 1970 *J. Fluid Mech.* **43**, 497–511.

STOLLERY, J. L. 1972 *AGARD Lecture Series* **42**, Vol. 1, Lecture 10.

STOLLERY, J. L. & BATES, L. 1974 *J. Fluid Mech.* **63**, 145–156.

VERMEULEN, J. P. & SIMEONIDES, G. 1992 *Von Karman Inst. Tech. Note* 181.

VINCENTI, W. G. & KRUGER, C. H. 1965 *Introduction to Physical Gasdynamics.* Wiley & Sons.

WHITE, F. M. 1974 *Viscous Fluid Flow.* McGraw–Hill.

WILKE, C. R. 1950 *J. Chem. Phys.* **18**, 517–519.

ZANCHETTA, M. 1996 Kinetic heating and transition studies at hypersonic speeds. PhD Thesis, University of London, UK.